The Astrophysical Journal, 956:39 (28pp), 2023 October 10 https://doi.org/10.3847/1538-4357/aceefd
© 2023. The Author(s). Published by the American Astronomical Society.
OPEN ACCESS

CLASSY VII Lyα Profiles: The Structure and Kinematics of Neutral Gas and Implications for LyC Escape in Reionization-era Analogs*

Weida Hu[1], Crystal L. Martin[1], Max Gronke[2], Simon Gazagnes[3], Matthew Hayes[4], John Chisholm[3], Timothy Heckman[5], Matilde Mingozzi[6], Namrata Roy[5], Peter Senchyna[7], Xinfeng Xu[5], Danielle A. Berg[3], Bethan L. James[8], Daniel P. Stark[9], Karla Z. Arellano-Córdova[3], Alaina Henry[5,6], Anne E. Jaskot[10], Nimisha Kumari[8], Kaelee S. Parker[3], Claudia Scarlata[11], Aida Wofford[12], Ricardo O. Amorín[13,14], Naunet Leonhardes-Barboza[15], Jarle Brinchmann[16], Cody Carr[11], and Alessandra Aloisi[6]
[1] Department of Physics, University of California, Santa Barbara, Santa Barbara, CA 93106, USA
[2] Max-Planck Institute for Astrophysics, Karl-Schwarzschild-Str. 1, D-85741 Garching, Germany
[3] Department of Astronomy, The University of Texas at Austin, 2515 Speedway, Stop C1400, Austin, TX 78712, USA
[4] Stockholm University, Department of Astronomy and Oskar Klein Centre for Cosmoparticle Physics, AlbaNova University Centre, SE-10691, Stockholm, Sweden
[5] Center for Astrophysical Sciences, Department of Physics & Astronomy, Johns Hopkins University, Baltimore, MD 21218, USA
[6] Space Telescope Science Institute, 3700 San Martin Drive, Baltimore, MD 21218, USA
[7] Carnegie Observatories, 813 Santa Barbara Street, Pasadena, CA 91101, USA
[8] AURA for ESA, Space Telescope Science Institute, 3700 San Martin Drive, Baltimore, MD 21218, USA
[9] Steward Observatory, The University of Arizona, 933 N Cherry Avenue, Tucson, AZ 85721, USA
[10] Department of Astronomy, Williams College, Williams town, MA 01267, USA
[11] Minnesota Institute for Astrophysics, University of Minnesota, 116 Church Street SE, Minneapolis, MN 55455, USA
[12] Instituto de Astronomía, Universidad Nacional Autónoma de México, Unidad Académica en Ensenada, Km 103 Carr. Tijuana-Ensenada, Ensenada 22860, Mexico
[13] Instituto de Investigación Multidisciplinar en Ciencia y Tecnología, Universidad de La Serena, Raul Bitrán 1305, La Serena 2204000, Chile
[14] Departamento de Astronomía, Universidad de La Serena, Av. Juan Cisternas 1200 Norte, La Serena 1720236, Chile
[15] Wellesley College, 106 Central Street, Wellesley, MA 02481, USA
[16] Instituto de Astrofísica e Ciências do Espaço, Universidade do Porto, CAUP, Rua das Estrelas, PT4150-762 Porto, Portugal
Received 2023 April 17; revised 2023 July 11; accepted 2023 July 27; published 2023 October 5

Abstract

Lyα line profiles are a powerful probe of interstellar medium (ISM) structure, outflow speed, and Lyman-continuum escape fraction. In this paper, we present the Lyα line profiles of the Cosmic Origins Spectrograph (COS) Legacy Archive Spectroscopic SurveY, a sample rich in spectroscopic analogs of reionization-era galaxies. A large fraction of the spectra show a complex profile, consisting of a double-peaked Lyα emission profile in the bottom of a damped, Lyα absorption trough. Such profiles reveal an inhomogeneous ISM. We successfully fit the damped Lyα absorption and the Lyα emission profiles separately, but with complementary covering factors, a surprising result because this approach requires no Lyα exchange between high-$N_{\rm H\,I}$ and low-$N_{\rm H\,I}$ paths. The combined distribution of column densities is qualitatively similar to the bimodal distributions observed in numerical simulations. We find an inverse relation between Lyα peak separation and the [O III]/[O II] flux ratio, confirming that the covering fraction of Lyman-continuum-thin sightlines increases as the Lyα peak separation decreases. We combine measurements of Lyα peak separation and Lyα red peak asymmetry in a diagnostic diagram, which identifies six Lyman-continuum leakers in the COS Legacy Archive Spectrocopy SurveY (CLASSY) sample. We find a strong correlation between the Lyα trough velocity and the outflow velocity measured from interstellar absorption lines. We argue that greater vignetting of the blueshifted Lyα peak, relative to the redshifted peak, is the source of the well-known discrepancy between shell-model parameters and directly measured outflow properties. The CLASSY sample illustrates how scattering of Lyα photons outside the spectroscopic aperture reshapes Lyα profiles because the distances to these compact starbursts span a large range.

Unified Astronomy Thesaurus concepts: Dwarf galaxies (416); Hubble Space Telescope (761); Stellar feedback (1602); Interstellar medium (847)

Supporting material: figure set, machine-readable tables

1. Introduction

The Epoch of Reionization (EoR) marks a period in the history of the Universe when the emergence of galaxies ionized most of the neutral hydrogen in the intergalactic medium (IGM). Observations suggest that the first ionized pockets in the IGM grew around the largest overdensities of galaxies (e.g., Tilvi et al. 2020; Hu et al. 2021; Hayes & Scarlata 2023). The massive stars in those galaxies are likely the source of the ionizing photons, the Lyman continuum (LyC) at wavelengths $\lambda < 912$ Å (e.g., Robertson et al. 2015). How this ionizing radiation leaks out of the dense structures where early galaxies form, however, is not well understood. A small column density of neutral hydrogen, $N_{\rm H\,I} \approx 1.6 \times 10^{17}$ cm^{-2}, will absorb a LyC photon. Exactly how feedback from massive stars opens pathways for LyC escape (Ma et al. 2020; Kakiichi & Gronke 2021) sets the timeline for

* Based on observations made with the NASA/ESA Hubble Space Telescope, obtained from the Data Archive at the Space Telescope Science Institute, which is operated by the Association of Universities for Research in Astronomy, Inc., under NASA contract NAS 5-26555.

Original content from this work may be used under the terms of the Creative Commons Attribution 4.0 licence. Any further distribution of this work must maintain attribution to the author(s) and the title of the work, journal citation and DOI.

cosmic reionization (e.g., Finkelstein et al. 2019; Mason et al. 2019; Naidu et al. 2020). Direct observations of the escaping LyC photons are not possible during the EoR because of attenuation by the IGM (Ouchi et al. 2020, and references therein), so indirect tracers of LyC escape, and outflows are needed.

Lyα is the most commonly detected emission line from high-redshift galaxies (Partridge & Peebles 1967). The channels through which Lyα photons emerge from galaxies appear to be tightly related to the pathways of LyC escape (Chisholm et al. 2018; Gazagnes et al. 2020) because the origins of Lyα photons, H II regions, are illuminated by the LyC photons arising from central massive stars. Even low-column densities of neutral hydrogen in these channels scatter Lyα photons many times, altering their direction and frequency. Their random walk redistributes photons flux from the line core into the line wings, and this reshaping of the line profile imprints information about the outflow velocity, column density, and interstellar medium (ISM) structure on the emergent line profile (Verhamme et al. 2006, 2015; Dijkstra 2014; Chisholm et al. 2018; Gazagnes et al. 2020; Saldana-Lopez et al. 2022).

In the absence of absorption by dust, all the Lyα photons eventually escape from the galaxy, and radiative transfer calculations demonstrate some general properties of the line profiles. For example, analytic solutions for static slabs and spheres yield emerging Lyα spectra with symmetric redshifted and blueshifted peaks (Neufeld 1990; Dijkstra et al. 2006, 2016). Bulk motion requires Monte Carlo techniques, and these calculations demonstrate that outflowing gas produces an asymmetric profile, which has a stronger redshifted component regardless of the outflow geometry and structure (Verhamme et al. 2006, 2012).

The most commonly applied radiative transfer model, the homogeneous shell model, assumes an expanding, spherical shell of neutral hydrogen (Verhamme et al. 2006). Over a wide range of outflow properties, the emergent line profile has a P Cygni shape characterized by a redshifted emission line with a broad red wing plus a blueshifted absorption trough. For a very low H I column density, some emission from the near side of the thin shell is transmitted, producing blueshifted emission instead of absorption. Whereas a very-high-column density shell will trap a Lyα photon until it is eventually absorbed by a dust grain, and the emergent line profile has become that of a damped Lyα absorber (DLA), a completely dark absorption trough with very broad wings. The shell model does a good job of reproducing the diversity of commonly observed Lyα profile shapes (e.g., Verhamme et al. 2015; Gronke et al. 2017; Yang et al. 2017; Gurung-López et al. 2022). Statistically successful fits, however, do not guarantee an accurate recovery of outflow properties. The structure of the shell model is much simpler than actual ISM and multiphase outflows (Schneider & Robertson 2018; Gronke & Oh 2020; Fielding & Bryan 2022).

Low-ionization state (LIS) absorption lines in galaxy spectra unambiguously detect outflowing gas and have provided insight into how outflow properties vary with galaxy properties (Heckman et al. 2000, 2011; Martin et al. 2012, 2015; Chisholm et al. 2015). The outflow speeds derived from the blueshifts of these absorption lines offer an opportunity to test the shell model velocities, and the results reveal significant discrepancies both at high-redshift (Kulas et al. 2012) and among nearby Green Pea galaxies (Yang et al. 2017; Orlitová et al. 2018). Three major discrepancies are reported in those studies: (1) the best-fit redshifts are larger by 10–250 km s^{-1} than the spectroscopic redshifts; (2) the best-fit outflow velocities of expanding shell are lower than the outflow velocities derived by LIS lines; (3) the intrinsic Lyα line widths of shell model are broader than those of Balmer lines. Li & Gronke (2022) proposed that those discrepancies might be caused by the degeneracies between model parameters, but no explanation for these puzzles based on observations has been found.

We also draw attention to another limitation of the shell model. A large fraction of Green Peas and higher-redshift star-forming galaxies show Lyα emission line in the bottom of a DLA system (Reddy et al. 2016; McKinney et al. 2019). These profiles cannot be produced by a homogeneous shell model. The low-column density shells that produce double-peaked profiles contradict the presence of damped absorption, which requires very-high-column density. Even larger peak separations are predicted by a clumpy shell because the fitted shell expansion speed lies between the outflow velocities of the neutral clouds and the hot interclump medium (Li & Gronke 2022).

Comparing the physical properties derived from Lyα shell modeling to those measured from other spectral lines can therefore provide new insight about the structure of the multiphase gas. Because these properties determine the LyC escape fraction from galaxies, there is an urgent need to understand the puzzling properties of Lyα profiles in a sample of EoR analogs. To place the unexpected profile shapes, i.e., the double-peaked emission lines in DLA systems, in the broader context of the full diversity of observed Lyα profile shapes, requires high-resolution and high signal-to-noise ratio (S/N) UV spectroscopy of EoR analogs, including, but not limited to, Green Pea galaxies. The James Webb Space Telescope (JWST) observations reveal a diversity of galaxies in the EoR (e.g., Labbe et al. 2023; Bunker et al. 2023; Looser et al. 2023; Saxena et al. 2023; Tang et al. 2023), spanning much wider ranges of galaxy properties than those of the local Green Peas.

In this paper, we analyze 45 Lyα line profiles obtained by the Cosmic Origins Spectrograph (COS) Legacy Archive Spectrocopy SurveY (CLASSY; Berg et al. 2022; James et al. 2022). This UV-surface brightness selected sample includes the lowest-redshift Green Pea galaxies, local Lyman break galaxy analogs (LBAs; Heckman et al. 2011), and the two local galaxies that are the nearest spectral match to the emission-line spectra of GN-z11 (Senchyna et al. 2023). Thus, the range in metallicity and ionizing continuum properties include the extreme conditions that were common during galaxy assembly. We present a uniform analysis of the Lyα profiles. The outflow properties have been determined from the blueshifted components of the LIS resonance lines (Xu et al. 2022) and the excited fine-structure lines (Xu et al. 2023). The results provide new insight into the clumpiness of the ISM, as described by the relative covering fractions of high-$N_{\rm H\,I}$ and low-$N_{\rm H\,I}$ gas, yet also strongly suggest that the discrepancies between shell-model parameters and LIS absorption lines arise from aperture vignetting. Among CLASSY targets, the physical size of COS aperture ranges from the scale of star clusters ($\sim$100 pc) to galaxies ($\sim$10 kpc). The large variations in aperture losses make it possible to view individual Lyα profile shapes in a broader context.

This paper is organized as follows. In Section 2, we introduce the CLASSY sample of Lyα profiles, describe how we remove the damped Lyα absorption and measure the properties of the high-column density neutral gas, and discuss the large variation in the amount of aperture vignetting across

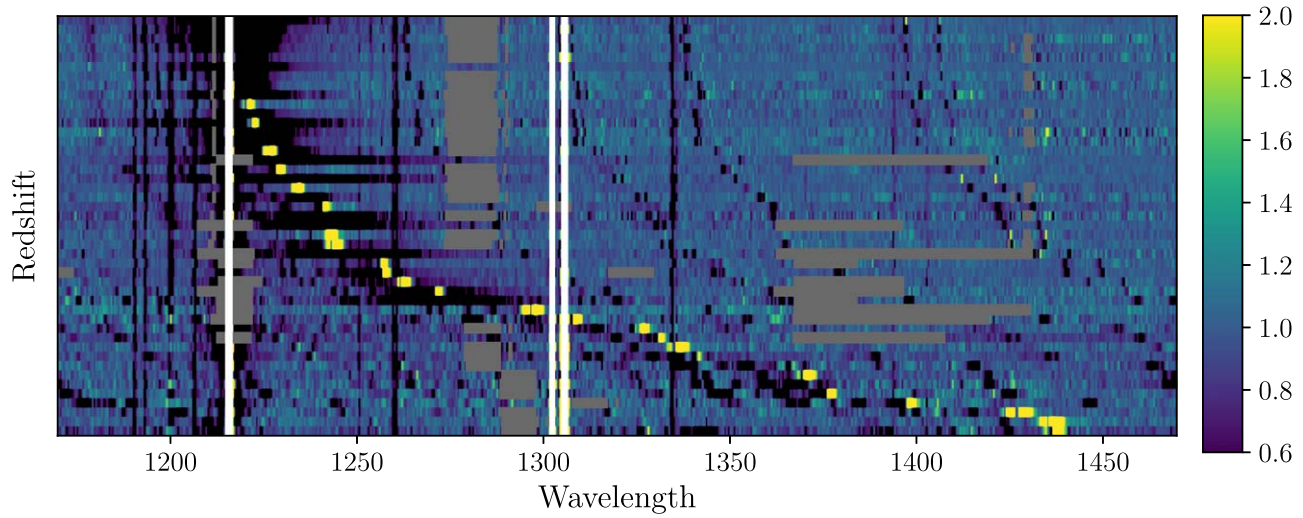

Figure 1. Overview of the COS G130M spectra obtained in the CLASSY survey with the wavelength coverage of 1170–1470 Å on the *x*-axis. The image is built by one continuum-normalized spectrum per image line. The redshift increases from top to bottom along the *y*-axis. The dark is low flux, and the yellow is high flux. The yellow waterfall highlights the redshifted Lyα emission lines. We use vertical white lines to mask the geocoronal Lyα and O II emission lines. The vertical dark lines indicate the MW absorption lines, and the gray strips indicate the CCD gaps.

the sample. In Section 3, we use the radiative transfer code tlac to fit shell models to the net Lyα emission-line profiles, investigating different choices for the continuum level (and hence the line equivalent width). In Section 4, we discuss the H I column density distribution in EoR analogs, the size scale of the holes leaking LyC radiation, and argue that the aperture vignetting biases the shell model properties in the directions required to solve the discrepancies with independently measured outflow properties.

Throughout this paper, we adopt a Flat ΛCDM cosmology with $\Omega_m = 0.3$, $\Omega_\Lambda = 0.7$, and $H_0 = 70$ km s^{-1} Mpc^{-1}. We also adopt the Spearman rank method to quantify the correlation strengths r. The data used in this paper are available via the CLASSY high-level science products (HLSP) homepage,[17] including the best-fit DLA systems, the Lyα emission lines after subtracting the DLA and continuum, and the best-fit shell model spectra.

2. Sample of Lyα Profiles

Here, we present high-S/N Lyα spectra for the 45 CLASSY targets. Each of these nearby galaxies has a compact, far-UV bright star-forming region, which was the target of the COS observation. The sample provides a diverse set of local analogs of high-redshift galaxies, including both Green Pea galaxies and LBAs. The physical conditions in the starburst range cover oxygen abundances from $12 + \log(\mathrm{O/H}) \sim 7$ to 8.8 and electron densities from $n_e \sim 10$ to 1120 cm^{-3}. The stellar masses and star formation rates of their host galaxies sample the range $\log(M_\star/M_\odot) \sim 6.2$ to 10.1 and $\log(\mathrm{SFR}/M_\odot\ \mathrm{yr}^{-1}) \sim -2$–1.6, respectively (Berg et al. 2022). The raw spectroscopic data were reduced using the CALCOS pipeline (v3.3.10), including spectrum extraction, wavelength calibration, and vignetting correction, and then coadded using a custom pipeline (James et al. 2022). The Galactic foreground extinction was corrected assuming a ratio of total-to-selective extinction $R_V = 3.1$ and a Milky Way (MW) extinction curve (Cardelli et al. 1989).

[17] The data is available at the CLASSY HLSP page at DOI:10.17909/m3fq-jj25 and https://archive.stsci.edu/hlsp/classy.

Figure 1 shows an overview of the G130M and G160M spectra, ordered by redshift. The CLASSY spectra easily resolve the damping wings of the broad absorption trough imprinted by H I absorption from the MW. A large fraction of the spectra show a second DLA at the redshift of the CLASSY galaxy. In the lowest-redshift galaxies, the blueshifted damping wing of the target is blended with the redshifted damping wing of the MW absorption. The yellow waterfall across Figure 1 highlights the redshifted Lyα emission. Surprisingly, the Lyα emission is frequently detected in the bottom of a damped absorption trough. Profiles of this type cannot be produced by a uniform shell of neutral hydrogen.

In this paper, we adopt an approach that we have not seen used previously. We fit the damping wing profile, including a nonunity covering factor. We then extract the net emission-line profile relative to the damping trough, as others have done. The equivalent width of this net Lyα emission, however, has been previously neglected. We address this in Section 3.2 below, where we demonstrate that the best normalization for the Lyα emission is the fraction of the stellar continuum *not intercepted* by the high-column density neutral hydrogen.

We use physical models to define the continuum level near Lyα, allowing us to accurately model the DLA system in Section 2.1. CLASSY provides two models for the continuum (P. Senchyna et al. 2023, in preparation). Both models assume the observed continuum can be reconstructed as a linear combination of a set of single-age, single-metallicity stellar populations (Chisholm et al. 2019), and, thus, be fitted using the following relation:

$$F_{\mathrm{obs}}(\lambda) = 10^{-0.4E(B-V)k(\lambda)} \Sigma_i\, X_i M_i(\lambda), \quad (1)$$

where $F_{\mathrm{obs}}(\lambda)$ is the observed spectrum, $k(\lambda)$ is the attenuation law, $M_i(\lambda)$ is the spectrum of the ith single stellar population, and X_i is its coefficient. The main difference between the two methods is the stellar population synthesis framework. The top panels of Figure 2 illustrate each best-fit continuum. The red dashed line represents the continuum built from STARBURST 99 synthesis models (Leitherer et al. 1999) and

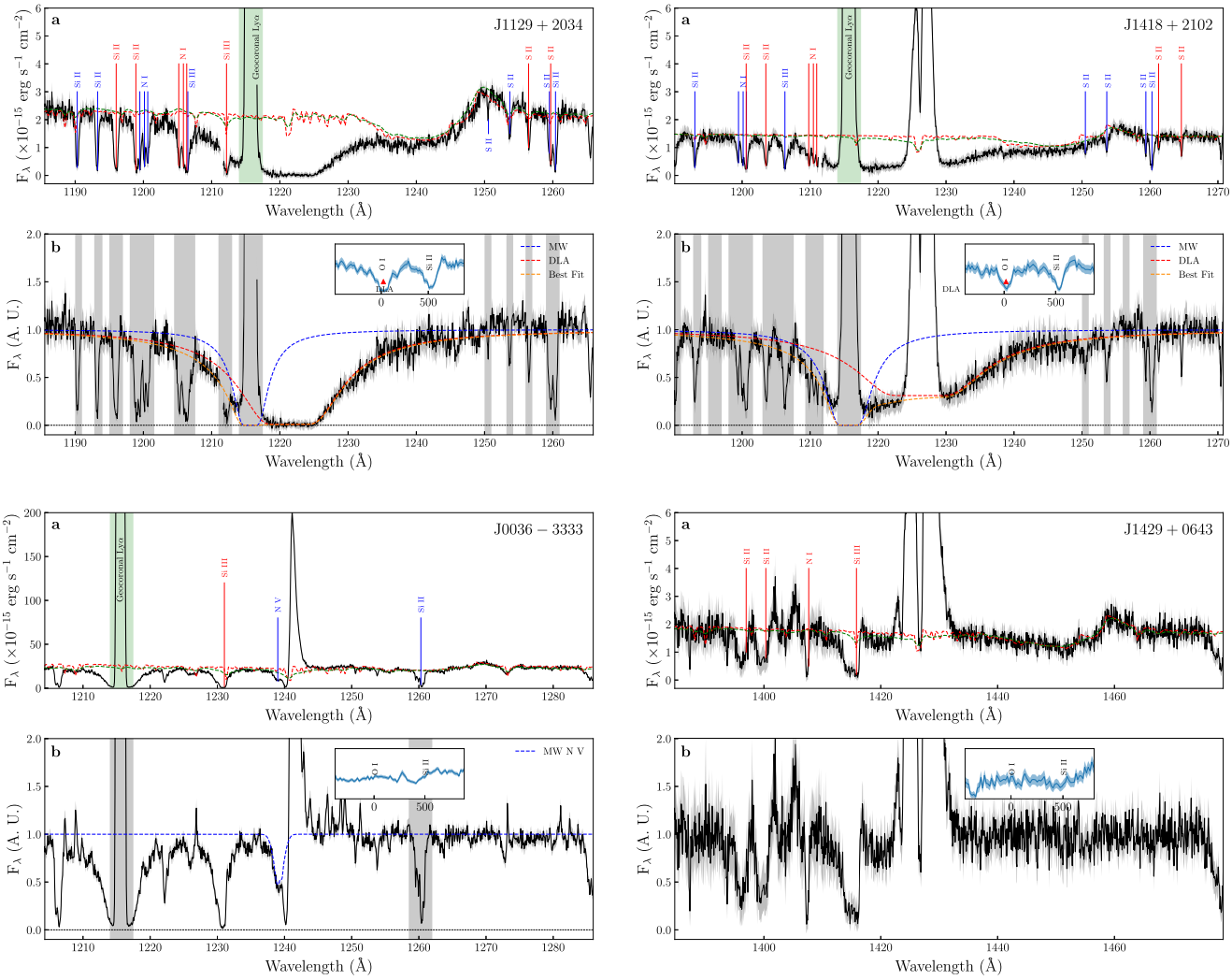

Figure 2. Examples of four typical Lyα profiles: pure DLA system, Lyα emission over DLA system, P Cygni–like Lyα emission, and pure Lyα emission. Panel (a): the flux spectra (black) and error spectra (gray shade) close to Lyα line. The vertical green shade masks the geocoronal Lyα emission line. The absorption lines are labeled in blue and red for absorption lines of MW and host galaxy, respectively. We overplot the best-fit continua in red and green dashed lines for the first and second methods (see Section 2), respectively. Panel (b): the best-fit absorption profiles (orange). The flux spectrum and error spectrum are normalized by the best-fit continuum (first method, red dashed line in panel (a)). We mask the absorption lines (vertical gray shades) and Lyα emission line and use two components to fit the absorption profile, which corresponds to the MW component (blue) and a host-galaxy DLA component (red). For the host-galaxy component, we adopt a Voigt profile. For the MW component, we adopt a Voigt profile if it is an MW DLA system with fixed galactic H I column density (Hartmann & Burton 1997), or a Gaussian profile if it is an MW metal absorption line. The small inset shows the O I λ1302 Å absorption line.

(The complete figure set of 45 images is available.)

a Reddy et al. (2016) attenuation law, and the green dashed line uses the latest version of the Bruzual & Charlot (2003) model (S. Charlot & G. Bruzual 2023, in preparation; see also Plat et al. 2019) and an SMC extinction law (Gordon et al. 2003). These two continua both reproduce the prominent N V λ1240 stellar P Cygni line well. The narrow dip visible at Lyα in both models is not physical (C. Leitherer 2023, private communication), and we interpolate over it. We fit the DLA profiles using both the continuum models and found similar parameters. We adopt the first method for the analysis that follows because the STARBURST99 models have the higher spectral resolution.

2.1. DLA Fitting

Figure 2 illustrates the diversity of CLASSY Lyα profiles: pure DLA systems, Lyα emission in the bottom of a damping trough (hereafter Abs+EM profile), P Cygni–like profiles, and double-peaked Lyα emission. A large fraction of CLASSY spectra (31/45) have a DLA system, and 20 out of these 31 galaxies show double- or single-peaked Lyα emission lines. CLASSY spectra offer the high spectral resolution and S/N required to remove the contribution of the DLA system (e.g., Reddy et al. 2016; McKinney et al. 2019) and extract the Lyα emission lines.

Figure 1 shows that geocoronal emission lines intersect the broad damping wings at low-redshift and at $z \approx 0.07$. In addition, the LIS absorption lines from the MW and the target galaxy affect the wings of the DLA systems but intersect only a few Lyα emission lines (see Section 2.1.2). We mask these lines as indicated in the second row of Figure 2.

To uniquely describe the MW DLA system, we adopt the Galactic H I column density derived from 21 cm emission in the direction of the target (Hartmann & Burton 1997). The

DLA line profile is described by a Voigt profile (e.g., Prochaska 2019), which is defined by a Doppler parameter (b) and a column density ($N_{\rm H\,I}$). We assume a Doppler parameter of 30 km s^{-1} (e.g., Prochaska et al. 2015), no velocity shift, and complete covering of the continuum source. These steps define the Voigt profile, which we convolve with the instrumental resolution, and then subtract from the normalized continuum to uncover the Lyα profile of the CLASSY target.

Because DLA systems are optically thick, the bottom of the Voigt profile is completely dark. However, we found significant residual intensity in the bottom of the damping troughs. A partial covering of the continuum source therefore turns out to be critical for fitting damping profiles. This partial covering was sometimes subtle, as in the top left panel (J1129+2034) of Figure 2. In contrast, the top right panel (J1418+2102) of Figure 2 shows strong H I damping wings and prominent residual intensity in the trough. Here, we adopt a modified Voigt profile, which allows a velocity offset, v, and a velocity-independent covering fraction, f_C.

We convolve each Voigt profile with a Gaussian line spread function whose width is determined by the spectral resolution (Table 3 in Berg et al. 2022). Our fitting code then multiplies the normalized continuum by the optical depth of each Voigt profile. The error is measured using a Monte Carlo (MC) approach; we add random noise to the observed spectra and refit it 1000 times. Leaving all the parameters free provided statistically good fits; however, we noticed degeneracies between the fitted velocity v of the DLA and the wings of the damping profile, and also the overlaps between the wings of the DLA system and Lyα emission.

We broke these degeneracies by using the O I λ1302.2 Å absorption line to constrain the parameters of the Voigt profile, an approach Section 2.1.1 justifies below. The profile shape is not sensitive to b, and we fixed b to be 30 km s^{-1}. The second row of Figure 2 presents the continuum-normalized spectra, our model for the MW absorption, and the fitted damped Lyα absorption. Table 1 summarizes the best-fit Voigt parameters for the DLAs.

We extract the Lyα emission lines by subtracting the stellar continuum and DLA profile. Previous works have visually selected a local continuum close to the Lyα emission. A comparison of common targets shows that the resulting Lyα can be sensitive to the wavelength range used to define the local continuum. For example, the beginning of the wavelength range of J0938+5428 used in Alexandroff et al. (2015) is the Lyα blue peak of J0938+5428 in Figure 2. For this same target, Yang et al. (2017) determine the wavelength range from the intersection of the Lyα emission line with the DLA profile. This method recovers the Lyα blue peak; however, it underestimates the Lyα flux because the bottom of the DLA system is poorly estimated.

Among 45 CLASSY galaxies, 24 galaxies show significant double-peak Lyα emission lines, and 10 show single-peak Lyα emission. Figure 3 presents the Lyα emission-line spectra of 34 CLASSY galaxies. The remaining 11 galaxies show pure DLA systems, and are therefore not included in Figure 3.

2.1.1. Constraining the DLA Properties with O I Absorption

We use the narrow O I absorption lines to constrain the velocity of the DLA. Since the ionization potentials of O and H are very similar, we expect the O I to trace H I gas in the DLA absorber. Figure 4 validates this expectation; the DLA systems in CLASSY always associate with strong O I absorption. The only O I absorber without a DLA is J1112+5503, which shows a P Cygni Lyα profile still suggesting substantial H I gas.

For optically thick O I absorption, the residual flux at the bottom of the fitted Gaussian profile determines the covering fraction of O I gas. The O I optical depth can be measured following

$$\tau = 0.318\left(\frac{N_{\rm O\,I}}{10^{14}\ {\rm cm}^{-2}}\right)\left(\frac{30\ {\rm km\ s}^{-1}}{b}\right), \quad (2)$$

where $N_{\rm O\,I}$ is the O I column density, and b is the Doppler parameter (Draine 2011). Since the H I column densities of DLAs in the CLASSY sample are $>10^{20}$ cm^{-2}, and the metallicities 12+log(O/H) are >7.5, we find that the O I optical depths are >10, and the line is saturated. We acknowledge that this argument relies on the assumption that O I is uniformly distributed in the neutral gas. If the intervening O I clouds have different velocities, the covering fraction derived from O I absorption would place a lower limit on the covering fraction of neutral gas (Rivera-Thorsen et al. 2015).

Figure 5 shows that the O I covering fraction is approximately equal to the covering fraction of the DLA system. Table 1 collects the best-fit velocities and covering fractions for the DLA and O I absorption.

2.1.2. Notes on Individual Galaxies

1. The bottom of the DLA system is hidden under the Lyα emissions in J0938+5428, J1024+0524, J1416+1223, and J1521+0759 in their plots; see the online component of Figure 2, so the residual flux in the damping trough is not directly constrained. Since the blue wing of the damping profile is contaminated by metal absorption lines, the shape of the damping profile is poorly constrained. Therefore, for these four galaxies, we adopt the O I covering fractions to be their DLA covering fractions.
2. The covering fractions of four galaxies (J0337-0502, J0405-3648, J1132+1411, J1448-0110) are fixed to be a constant measured visually but also in agreement with their O I covering fractions. The Voigt profile fit for these four galaxies underestimates the covering fraction because the CLASSY error spectra do not account for the small counts at the trough bottom, which produce an asymmetric error (Cash 1979).
3. The DLA systems of three galaxies (J0127-0619, J1044+0353, J1359+5726) were not fitted well by a single Voigt profile, and we noticed that their O I absorption lines show a second component. Thus, we adopted two Voigt profiles and matched their velocities and covering factors to those of the O I components.
4. In J1105+4444, the Lyα peak separation is exceptionally broad, $\sim$1000 km s^{-1}. We suggest that the peaks are likely emitted by different regions within the COS aperture. To test this conjecture, we inspected Hubble Space Telescope (HST)/COS NUV acquisition image (see Figure 3 in Berg et al. 2022). We found that J1105+4444 is not only an elongated object with multiple clumps, but also the major axis of these clumps is along the dispersion direction of the COS observation. Thus, their spatial offset in the aperture may cause an apparent

Table 1
DLA Measurements

Object	z_{spec}	D_L[a] (Mpc)	$f_{c,DLA}$	$f_{c,O\ I}$	$\log N_H$ (cm^{-2})	v (km s^{-1})	COS Aperture Size (kpc)
(1)	(2)	(3)	(4)	(5)	(6)	(7)	8
J0021+0052	0.09839	452	...	...	...	...	4.5
J0036-3333	0.02060	80	...	...	...	...	0.93
J0127-0619	0.00540	18	0.08 ± 0.04	0.38 ± 0.15	21.21 ± 0.27	-189 ± 14	0.22
			0.92 ± 0.04	0.93 ± 0.06	21.04 ± 0.03	11 ± 5	
J0144+0453	0.00520	17	0.96 ± 0.01	0.78 ± 0.05	20.18 ± 0.02	42 ± 7	0.2
J0337-0502	0.01352	51	1.00	0.76 ± 0.03	21.81 ± 0.00	-18 ± 3	0.61
J0405-3648	0.00280	11	>0.99	...[d]	20.80 ± 0.02	-35 ± 17[b]	0.13
J0808+3948	0.09123	417	...	...	...	...	4.2
J0823+2806	0.04722	210	0.99 ± 0.01	0.98 ± 0.02	21.61 ± 0.03	22 ± 20	2.3
J0926+4427	0.18067	875	...	...	...	...	7.6
J0934+5514	0.00250	12	0.98 ± 0.00	0.38 ± 0.02[d]	21.24 ± 0.00	23 ± 3	0.14
J0938+5428	0.10210	471	0.80 ± 0.05[c]	0.80 ± 0.05	20.34 ± 0.08	3 ± 13	4.7
J0940+2935	0.00168	10	0.95 ± 0.01	0.69 ± 0.06[d]	21.26 ± 0.01	-51 ± 7	0.12
J0942+3547	0.01486	65	...	...	...	...	0.76
J0944-0038	0.00478	24	0.84 ± 0.03	0.88 ± 0.15	21.67 ± 0.05	7 ± 24	0.29
J0944+3442	0.02005	86	0.92 ± 0.01	0.85 ± 0.11	21.51 ± 0.03	13 ± 23	1
J1016+3754	0.00388	20	...	...	...	...	0.24
J1024+0524	0.03319	143	0.54 ± 0.05[c]	0.54 ± 0.05	20.58 ± 0.07	-72 ± 13	1.6
J1025+3622	0.12650	593	0.47 ± 0.12	0.56 ± 0.05	20.69 ± 0.19	-151 ± 34	5.7
J1044+0353	0.01287	60	0.09 ± 0.03	0.50 ± 0.09	20.08 ± 0.44	-101 ± 75	0.71
			0.91 ± 0.03	0.91 ± 0.05	21.84 ± 0.03	-29 ± 9	
J1105+4444[e]	0.02154	92	0.42 ± 0.07	...	20.88 ± 0.09	-121 ± 31	1.1
			0.58 ± 0.07	...	21.87 ± 0.07	-54 ± 85	
J1112+5503	0.13164	619	...	...	...	...	5.9
J1119+5130	0.00446	22	0.80 ± 0.02	0.68 ± 0.04	20.77 ± 0.03	-2 ± 8	0.26
J1129+2034	0.00470	27	0.99 ± 0.01	0.87 ± 0.04	21.11 ± 0.01	23 ± 5	0.32
J1132+5722	0.00504	24	1.00 ± 0.01	0.71 ± 0.11	21.24 ± 0.02	17 ± 15	0.29
J1132+1411	0.01764	74	1.00	0.98 ± 0.01	20.53 ± 0.01	-40 ± 4	0.87
J1144+4012	0.12695	595	0.92 ± 0.03	0.91 ± 0.03	20.52 ± 0.06	-225 ± 36	5.7
J1148+2546	0.04512	195	0.78 ± 0.02	0.93 ± 0.06	21.19 ± 0.03	-75 ± 11	2.2
J1150+1501	0.00245	11	0.89 ± 0.00	0.81 ± 0.03[d]	21.04 ± 0.01	10 ± 5	0.13
J1157+3220	0.01097	52	...	...	...	...	0.62
J1200+1343	0.06675	300	...	...	...	...	3.2
J1225+6109	0.00234	10	0.96 ± 0.01	...[d]	21.26 ± 0.01	11 ± 5[b]	0.12
J1253-0312	0.02272	100	0.47 ± 0.01	0.62 ± 0.04	21.41 ± 0.04	-45 ± 6	1.2
J1314+3452	0.00288	12	0.95 ± 0.01	0.92 ± 0.02[d]	20.71 ± 0.01	-39 ± 2	0.15
J1323-0132	0.02246	93	...	...	...	...	1.1
J1359+5726	0.03383	140	0.56 ± 0.4	0.50 ± 0.02	20.07 ± 0.11	-306 ± 17	1.6
			0.34 ± 0.1	0.82 ± 0.04	21.44 ± 0.15	-106 ± 10	
J1416+1223	0.12316	576	0.80 ± 0.05[c]	0.80 ± 0.05	20.19 ± 0.05	16 ± 13	5.5
J1418+2102	0.00855	40	0.70 ± 0.02	0.79 ± 0.07	21.30 ± 0.03	18 ± 6	0.48
J1428+1653	0.18167	881	...	...	...	...	7.6
J1429+0643	0.17350	837	...	...	...	...	7.4
J1444+4237	0.00230	9	0.98 ± 0.00	0.44 ± 0.3[d]	21.57 ± 0.01	-46 ± 8	0.11
J1448-0110	0.02741	111	>0.99	0.95 ± 0.03	21.56 ± 0.01	23 ± 5	1.3
J1521+0759	0.09426	432	0.49 ± 0.06[c]	0.49 ± 0.06	20.42 ± 0.11	-85 ± 19	4.4
J1525+0757	0.07579	343	...	...	...	...	3.6
J1545+0858	0.03772	159	0.40 ± 0.02	0.63 ± 0.1	21.54 ± 0.04	-25 ± 12	1.8
J1612+0817	0.14914	709	...	...	...	...	6.5

Notes. (1) Object name; (2) spectroscopic redshift from Berg et al. (2022); (3) luminosity distance; (4) covering fraction of DLA absorber; (5) covering fraction of O I absorption; (6) column density of DLA absorber; (7) velocity of O I absorption line (except J1105+4444); (8) physical size of COS aperture.

[a] The luminosity distances have been corrected for cosmic flow using `Cosmicflows-3` model http://edd.ifa.hawaii.edu/ (Kourkchi et al. 2020). We adopt the CF3 model, as it considers several mass concentrations, including the Virgo Cluster, the Great Attractor, etc., and provides distance–velocity relation for every random galaxy at distance within 200 Mpc.

[b] The velocity of O I absorber is measured using C II absorption line.

[c] The covering fraction of DLA absorber is measured using O I absorption line.

[d] The covering fraction of O I might be underestimated due to contamination of geocoronal O I emission line.

[e] The Voigt parameters of J1105+4444 are fitted using two free velocities. For more details, see Section 2.1.2.

(This table is available in machine-readable form.)

Table 2
Lyα Measurements

Object	$f_{Ly\alpha}$ (10^{-15} erg s^{-1} cm^{-2})	$\log L_{Ly\alpha}$ (erg s^{-1})	$EW_{Ly\alpha}$ (Å)	$f_{esc}^{Ly\alpha}$ (%)	A_f	$\Delta v_{Ly\alpha}$ (km s^{-1})	$v_{Ly\alpha}^{blue}$ (km s^{-1})	$v_{Ly\alpha}^{red}$ (km s^{-1})	$v_{Ly\alpha}^{trough}$ (km s^{-1})	$f_{Ly\alpha}^{blue}$ (10^{-15} erg s^{-1} cm^{-2})	$f_{Ly\alpha}^{red}$ (10^{-15} erg s^{-1} cm^{-2})
(1)	(2)	(3)	(4)	(5)	(6)	(7)	(8)	(9)	(10)	(11)	(12)
Double Peaks											
J0021+0052	144.56 ± 1.43	42.5	29.04 ± 0.29	25 ± 0.45	2.91 ± 0.04	571 ± 54	−419 ± 53	152 ± 12	−27 ± 20	8.4 ± 0.5	136.4 ± 1.4
J0808+3948	64.31 ± 0.52	42.1	15.02 ± 0.12	27 ± 0.22	1.29 ± 0.12	507 ± 28	−470 ± 26	37 ± 9	−312 ± 6	3.2 ± 0.2	61.2 ± 0.5
J0926+4427	64.64 ± 0.56	42.8	40.65 ± 0.35	35 ± 0.67	1.42 ± 0.13	427 ± 52	−203 ± 45	224 ± 25	−47 ± 17	7.5 ± 0.2	57.1 ± 0.5
J0938+5428	21.14 ± 0.52	41.7	4.06 ± 0.10	3.2 ± 0.083	1.93 ± 0.19	669 ± 52	−296 ± 41	373 ± 31	116 ± 32	7.4 ± 0.3	13.8 ± 0.4
J0942+3547	97.61 ± 0.31	40.7	17.95 ± 0.06	18 ± 0.093	1.53 ± 0.15	267 ± 16	−113 ± 14	154 ± 7	−16 ± 7	14.6 ± 0.3	82.6 ± 0.4
J0944-0038	20.47 ± 0.43	39.2	9.95 ± 0.21	4.1 ± 0.085	0.86 ± 0.35	416 ± 65	−150 ± 61	267 ± 23	34 ± 82	3.4 ± 0.7	17.1 ± 0.8
J0944+3442	0.43 ± 0.09	38.6	0.56 ± 0.11	0.82 ± 0.17	1.71 ± 0.59	531 ± 99	−273 ± 67	257 ± 76	−20 ± 150	0.1 ± 0.1	0.4 ± 0.1
J1016+3754	146.06 ± 1.74	39.8	15.42 ± 0.18	12 ± 0.16	1.51 ± 0.21	404 ± 45	−230 ± 43	175 ± 13	−34 ± 22	12.2 ± 0.9	133.9 ± 1.4
J1024+0524	54.13 ± 0.50	41.1	8.72 ± 0.08	5 ± 0.097	2.87 ± 0.08	464 ± 36	−338 ± 35	126 ± 8	−64 ± 18	2.1 ± 0.3	52.1 ± 0.5
J1025+3622	53.28 ± 0.62	42.3	21.95 ± 0.25	17 ± 0.25	1.70 ± 0.15	469 ± 43	−263 ± 39	206 ± 17	−100 ± 25	4.5 ± 0.2	48.8 ± 0.6
J1044+0353	1.55 ± 0.08	38.8	0.90 ± 0.05	0.096 ± 0.005	1.84 ± 0.36	425 ± 119	−293 ± 111	132 ± 45	−123 ± 98	0.2 ± 0.1	1.3 ± 0.1
J1105+4444	2.52 ± 0.18	39.4	0.53 ± 0.04	0.072 ± 0.0051	...	999 ± 109	−517 ± 76	482 ± 76	−204 ± 244	0.4 ± 0.2	2.2 ± 0.2
J1119+5130	2.30 ± 0.16	38.1	0.71 ± 0.05	0.78 ± 0.053	4.20 ± 0.27	649 ± 76	−337 ± 67	312 ± 34	−67 ± 108	1.2 ± 0.2	1.1 ± 0.1
J1148+2546	12.34 ± 0.23	40.7	5.62 ± 0.10	7.4 ± 0.14	1.92 ± 0.46	717 ± 97	−450 ± 73	268 ± 63	−132 ± 58	0.4 ± 0.1	12.0 ± 0.2
J1200+1343	80.54 ± 0.44	41.9	56.87 ± 0.31	9.3 ± 0.11	2.68 ± 0.05	530 ± 21	−394 ± 20	136 ± 5	−48 ± 20	9.0 ± 0.2	71.6 ± 0.4
J1253-0312	338.94 ± 1.21	41.6	32.14 ± 0.12	4.4 ± 0.032	1.48 ± 0.11	433 ± 14	−214 ± 11	219 ± 8	−46 ± 9	37.7 ± 0.5	301.1 ± 1.1
J1323-0132	190.14 ± 0.56	41.3	81.19 ± 0.24	21 ± 0.1	1.78 ± 0.06	168 ± 12	−95 ± 12	74 ± 1	−35 ± 7	45.0 ± 1.5	142.7 ± 1.5
J1416+1223	11.70 ± 0.47	41.7	3.26 ± 0.13	3 ± 0.13	1.75 ± 0.28	613 ± 91	−315 ± 80	298 ± 43	35 ± 51	6.0 ± 0.4	5.7 ± 0.3
J1418+2102	26.76 ± 0.22	39.7	19.14 ± 0.16	2.4 ± 0.021	1.10 ± 0.18	403 ± 26	−122 ± 25	281 ± 9	25 ± 9	7.6 ± 0.2	19.0 ± 0.2
J1428+1653	38.94 ± 0.82	42.6	12.32 ± 0.26	27 ± 1	3.34 ± 0.34	416 ± 84	−328 ± 76	89 ± 38	−109 ± 66	2.6 ± 0.3	36.4 ± 0.8
J1429+0643	67.53 ± 0.90	42.8	33.22 ± 0.44	11 ± 0.18	3.56 ± 0.15	545 ± 72	−292 ± 67	253 ± 25	54 ± 33	15.2 ± 0.5	52.4 ± 0.7
J1448-0110	0.43 ± 0.13	38.8	0.09 ± 0.03	0.027 ± 0.0083	...	395 ± 153	−354 ± 124	40 ± 91	−283 ± 134	0.1 ± 0.1	0.3 ± 0.1
J1521+0759	27.21 ± 0.64	41.8	4.85 ± 0.11	12 ± 0.52	3.27 ± 0.09	404 ± 48	−247 ± 45	157 ± 16	−68 ± 29	−1.0 ± 0.4	28.4 ± 0.7
J1545+0858	160.58 ± 1.02	41.7	29.26 ± 0.19	7.5 ± 0.048	2.75 ± 0.08	284 ± 14	−122 ± 10	163 ± 10	−27 ± 15	6.4 ± 0.3	154.2 ± 1.0
Single Peak / P Cygni											
J0036-3333	175.93 ± 1.20	41.1	7.13 ± 0.05	9.2 ± 0.063	...	...	...	100 ± 5	...	...	175.9 ± 1.2
J0940+2935	0.58 ± 0.06	36.8	0.34 ± 0.03	0.46 ± 0.044	...	...	...	273 ± 57	...	...	0.6 ± 0.1
J1112+5503	12.43 ± 0.45	41.8	5.45 ± 0.20	3.8 ± 0.15	...	...	...	143 ± 47	...	...	12.4 ± 0.4
J1144+4012	2.50 ± 0.21	41.0	1.75 ± 0.15	1.6 ± 0.14	...	...	...	318 ± 70	...	...	2.5 ± 0.2
J1157+3220	389.02 ± 2.53	41.1	21.63 ± 0.14	23 ± 0.2	...	...	...	50 ± 13	...	...	389.0 ± 2.5
J1225+6109	0.50 ± 0.21	36.8	0.04 ± 0.02	0.016 ± 0.0065	...	...	...	52 ± 63	...	...	0.5 ± 0.2
J1314+3452	0.85 ± 0.06	37.2	0.21 ± 0.01	0.027 ± 0.0018	...	...	...	210 ± 47	...	...	0.8 ± 0.1
J1359+5726	72.71 ± 0.68	41.2	8.71 ± 0.08	6.7 ± 0.081	...	...	...	148 ± 16	...	...	72.7 ± 0.7
J1525+0757	67.41 ± 1.21	42.0	14.92 ± 0.27	16 ± 0.43	...	...	...	82 ± 7	...	...	67.4 ± 1.2
J1612+0817	36.97 ± 0.83	42.3	12.71 ± 0.29	7 ± 0.18	...	...	...	114 ± 14	...	...	37.0 ± 0.8

Note. (1) Object name; (2) Lyα flux; (3) Lyα luminosity; (4) Lyα equivalent width; (5) Lyα escape fraction; (6) Lyα red peak asymmetry; (7) Lyα peak separation; (8) Lyα blue peak velocity offset; (9) Lyα red peak velocity offset; (10) Lyα trough velocity offset; (11) Lyα blue peak flux; (12) Lyα red peak flux. We note that the luminosity distances of some galaxies used in this work are different with those in Berg et al. (2022) because of the correction of cosmic flow. The properties (e.g., stellar mass, star formation rate) of those galaxies, which rely on the luminosities, are scaled accordingly.

(This table is available in machine-readable form.)

Table 3
Ancillary Data

Object	f_{1500} (10^{-15} erg s^{-1} cm^{-2})	M_{1500}	$Z_{\rm neb}$	$\log M_\star$ ($M_\odot$)	$E(B-V)$	O32	$v_{\rm Si\,II}^{\rm outflow}$ (km s^{-1})	r_{50} ($''$)
(1)	(2)	(3)	(4)	(5)	(6)	(7)	(8)	(9)
J0021+0052	3.94	−20.55	8.17 ± 0.07	$9.09^{+0.18}_{-0.38}$	0.13 ± 0.006	2.0 ± 0.1	231^{+77}_{-77}	0.25
J0036-3333	16.60	−18.34	8.21 ± 0.17	$9.09^{+0.26}_{-0.23}$	0.30 ± 0.012	1.1 ± 0.1	157^{+22}_{-22}	0.28
J0127-0619	4.04	−13.58	7.68 ± 0.02	$8.63^{+0.18}_{-0.15}$	0.48 ± 0.006	1.1 ± 0.1	...	0.15
J0144+0453	1.87	−12.63	7.76 ± 0.02	$7.52^{+0.24}_{-0.29}$	0.04 ± 0.030	2.1 ± 0.1	48^{+16}_{-16}	3.54
J0337-0502	7.99	−16.60	7.46 ± 0.04	$7.01^{+0.24}_{-0.21}$	0.05 ± 0.006	6.2 ± 0.2	...	1.62
J0405-3648	0.96	−10.90	7.04 ± 0.05	$6.60^{+0.28}_{-0.28}$	0.11 ± 0.005	0.6 ± 0.1	...	6.43
J0808+3948	3.42	−20.23	8.77 ± 0.12	$9.12^{+0.30}_{-0.17}$	0.24 ± 0.070	0.8 ± 0.1	646^{+65}_{-65}	0.08
J0823+2806	3.85	−18.86	8.28 ± 0.01	$9.38^{+0.33}_{-0.19}$	0.21 ± 0.004	2.0 ± 0.1	136^{+45}_{-45}	0.28
J0926+4427	1.14	−20.64	8.08 ± 0.02	$8.76^{+0.30}_{-0.26}$	0.10 ± 0.008	3.1 ± 0.1	353^{+52}_{-52}	0.23
J0934+5514	15.10	−14.05	6.98 ± 0.01	$6.25^{+0.15}_{-0.20}$	0.07 ± 0.007	8.7 ± 0.1	112^{+37}_{-37}	1.53
J0938+5428	3.56	−20.53	8.25 ± 0.02	$9.15^{+0.18}_{-0.29}$	0.13 ± 0.006	1.9 ± 0.1	215^{+72}_{-72}	0.28
J0940+2935	1.45	−11.14	7.66 ± 0.07	$6.80^{+0.23}_{-0.40}$	0.06 ± 0.010	0.7 ± 0.1	102^{+34}_{-34}	3.06
J0942+3547	3.80	−16.30	8.13 ± 0.03	$7.56^{+0.21}_{-0.29}$	0.06 ± 0.011	2.6 ± 0.1	97^{+26}_{-26}	0.33
J0944-0038	1.40	−13.07	7.83 ± 0.01	$6.89^{+0.44}_{-0.25}$	0.16 ± 0.010	2.9 ± 0.1	64^{+21}_{-21}	2.34
J0944+3442	0.69	−15.06	7.62 ± 0.11	$8.19^{+0.40}_{-0.23}$	0.16 ± 0.013	1.4 ± 0.1	...	3.74
J1016+3754	7.07	−14.43	7.56 ± 0.01	$6.77^{+0.27}_{-0.22}$	0.07 ± 0.012	4.6 ± 0.2	116^{+31}_{-31}	1.52
J1024+0524	4.50	−18.20	7.84 ± 0.03	$7.88^{+0.37}_{-0.24}$	0.10 ± 0.016	2.1 ± 0.1	94^{+12}_{-12}	0.40
J1025+3622	1.81	−20.30	8.13 ± 0.01	$8.87^{+0.25}_{-0.27}$	0.09 ± 0.006	2.4 ± 0.1	155^{+24}_{-24}	0.35
J1044+0353	1.70	−15.25	7.45 ± 0.03	$6.84^{+0.41}_{-0.26}$	0.08 ± 0.007	6.8 ± 0.1	52^{+12}_{-12}	0.38
J1105+4444	4.68	−17.28	8.23 ± 0.01	$8.98^{+0.29}_{-0.24}$	0.17 ± 0.005	2.0 ± 0.1	115^{+23}_{-23}	4.11
J1112+5503	1.91	−20.45	8.45 ± 0.06	$9.59^{+0.33}_{-0.19}$	0.23 ± 0.016	0.9 ± 0.1	349^{+107}_{-107}	0.20
J1119+5130	2.63	−13.54	7.57 ± 0.04	$6.81^{+0.15}_{-0.28}$	0.10 ± 0.008	2.0 ± 0.1	65^{+22}_{-22}	2.18
J1129+2034	1.87	−13.62	8.28 ± 0.04	$8.20^{+0.37}_{-0.27}$	0.23 ± 0.011	1.8 ± 0.1	51^{+17}_{-17}	0.38
J1132+5722	2.57	−13.69	7.58 ± 0.08	$7.32^{+0.23}_{-0.26}$	0.10 ± 0.008	0.8 ± 0.1	...	0.84
J1132+1411	1.75	−15.75	8.25 ± 0.01	$8.67^{+0.28}_{-0.19}$	0.13 ± 0.008	2.7 ± 0.1	60^{+10}_{-10}	8.86
J1144+4012	1.20	−19.86	8.43 ± 0.20	$9.89^{+0.18}_{-0.29}$	0.22 ± 0.010	0.6 ± 0.1	246^{+33}_{-33}	0.40
J1148+2546	2.07	−18.03	7.94 ± 0.01	$8.13^{+0.34}_{-0.24}$	0.10 ± 0.021	3.7 ± 0.1	95^{+19}_{-19}	1.31
J1150+1501	12.60	−13.71	8.14 ± 0.01	$6.83^{+0.28}_{-0.30}$	0.04 ± 0.004	2.3 ± 0.1	67^{+22}_{-22}	1.29
J1157+3220	14.40	−17.27	8.43 ± 0.02	$9.08^{+0.32}_{-0.18}$	0.08 ± 0.006	1.2 ± 0.1	238^{+49}_{-49}	2.89
J1200+1343	1.38	−18.53	8.26 ± 0.02	$8.12^{+0.47}_{-0.42}$	0.15 ± 0.006	5.1 ± 0.1	192^{+13}_{-13}	0.18
J1225+6109	9.50	−13.28	7.97 ± 0.01	$7.09^{+0.34}_{-0.24}$	0.11 ± 0.005	4.7 ± 0.1	51^{+17}_{-17}	2.91
J1253-0312	9.11	−18.19	8.06 ± 0.01	$7.66^{+0.51}_{-0.23}$	0.16 ± 0.008	8.0 ± 0.2	113^{+38}_{-38}	0.85
J1314+3452	3.72	−12.65	8.26 ± 0.01	$7.53^{+0.30}_{-0.21}$	0.14 ± 0.006	2.3 ± 0.1	62^{+21}_{-21}	0.30
J1323-0132	1.33	−15.94	7.71 ± 0.04	$6.29^{+0.26}_{-0.10}$	0.13 ± 0.042	37.8 ± 3.0	...	0.23
J1359+5726	6.34	−18.53	7.98 ± 0.01	$8.39^{+0.31}_{-0.26}$	0.09 ± 0.006	2.6 ± 0.1	161^{+23}_{-23}	1.10
J1416+1223	2.62	−20.63	8.53 ± 0.11	$9.59^{+0.32}_{-0.26}$	0.25 ± 0.008	0.8 ± 0.1	398^{+68}_{-68}	0.13
J1418+2102	1.17	−13.99	7.75 ± 0.02	$6.26^{+0.49}_{-0.35}$	0.08 ± 0.006	4.7 ± 0.1	51^{+7}_{-7}	0.40
J1428+1653	1.25	−20.75	8.33 ± 0.05	$9.56^{+0.15}_{-0.23}$	0.14 ± 0.008	1.2 ± 0.1	140^{+25}_{-25}	0.35
J1429+0643	1.62	−20.92	8.10 ± 0.03	$8.80^{+0.35}_{-0.21}$	0.12 ± 0.012	4.2 ± 0.2	230^{+51}_{-51}	0.15
J1444+4237	2.08	−11.33	7.64 ± 0.02	$6.39^{+0.17}_{-0.17}$	0.08 ± 0.053	4.1 ± 0.1	54^{+18}_{-18}	8.20
J1448-0110	4.08	−17.55	8.13 ± 0.01	$7.58^{+0.41}_{-0.24}$	0.15 ± 0.005	8.0 ± 0.1	145^{+43}_{-43}	0.23
J1521+0759	3.52	−20.33	8.31 ± 0.14	$9.00^{+0.29}_{-0.30}$	0.15 ± 0.008	1.5 ± 0.1	161^{+54}_{-54}	0.28
J1525+0757	3.52	−19.83	8.33 ± 0.04	$10.06^{+0.28}_{-0.42}$	0.25 ± 0.008	0.5 ± 0.1	408^{+28}_{-28}	0.25
J1545+0858	4.37	−18.40	7.75 ± 0.03	$7.50^{+0.43}_{-0.26}$	0.11 ± 0.036	8.6 ± 0.3	113^{+33}_{-33}	0.33
J1612+0817	2.70	−21.12	8.18 ± 0.19	$9.78^{+0.28}_{-0.26}$	0.29 ± 0.008	0.7 ± 0.1	459^{+63}_{-63}	0.20

Note. (1) Object name; (2) UV flux at 1500 Å from Berg et al. (2022); (3) UV absolute magnitude at 1500 Å; (4) metallicity from Berg et al. (2022); (5) stellar mass; (6) dust extinction from Berg et al. (2022); (7) O32 ratio; (8) velocity of Si II absorption line; (9) half-light radius from Xu et al. (2022).

(This table is available in machine-readable form.)

velocity shift, which is not physical. This object is excluded in the following analysis. For completeness, we note that the DLA fit for J1105+4444 failed when constrained by two O I components, and we used a double-Voigt profile with free velocities.

5. The blue part of the J1525+0757 Lyα line is likely a P Cygni profile, so the impact of the geocoronal O I emission should be negligible.
6. We also exclude J1448-0110 from the Lyα emission analysis due to the low S/N.

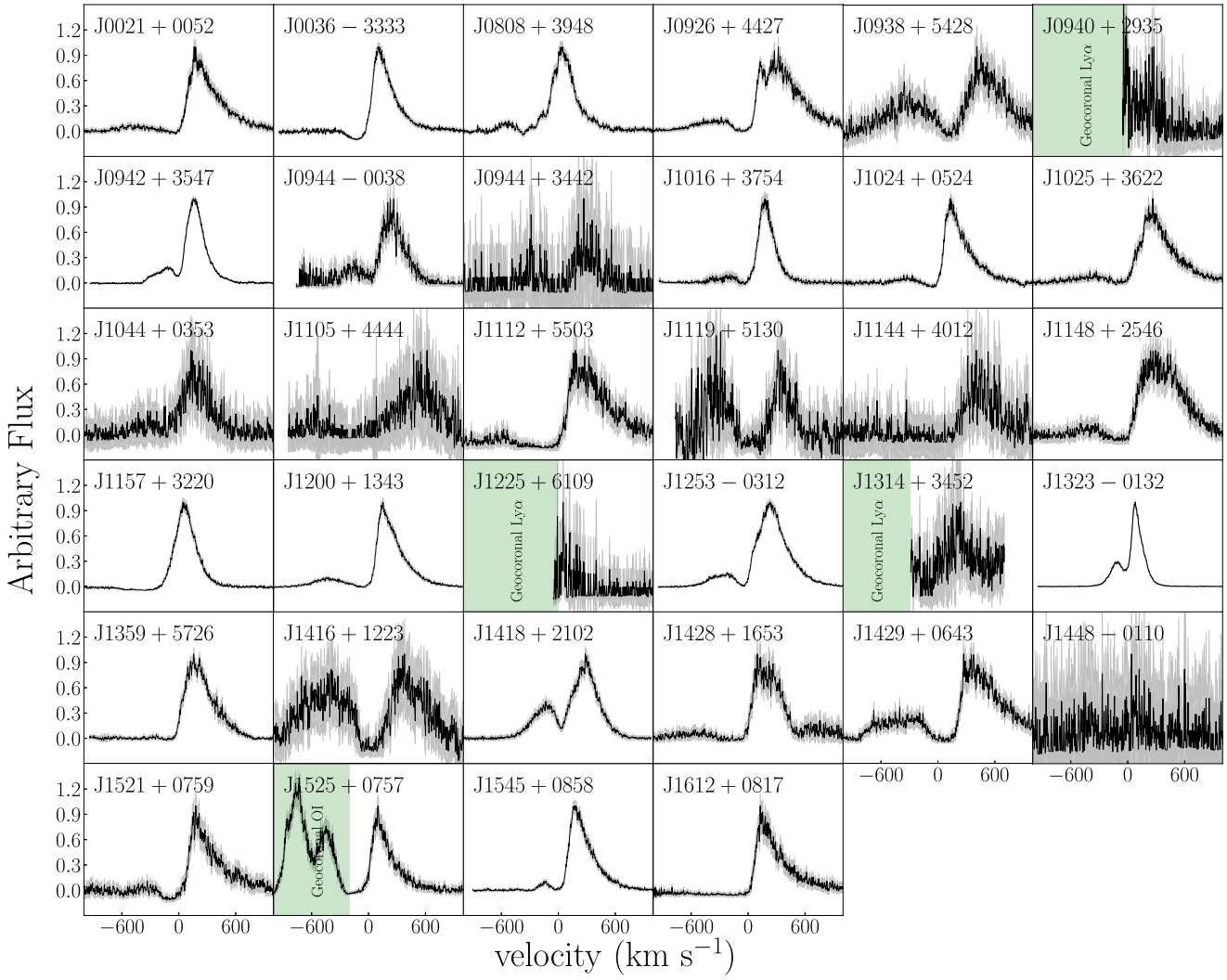

Figure 3. The Lyα spectra (black) and error spectra (gray) after subtracting the continuum and DLA of 34 CLASSY galaxies. We use green shades to show the masked geocoronal Lyα and O I emission lines. The continuum-subtracted spectra are normalized by peak flux. The total Lyα fluxes are measured by integrating fluxes within the wavelength range where Lyα emission lines meet zero flux.

2.2. DLA System and Aperture Loss

The fraction of emitted Lyα photons captured by the 2.″5 diameter COS aperture will vary dramatically among the targets because of their large range of distances. For a typical target, the physical diameter of the aperture is roughly 700 pc, which is larger than the half-light radius of the UV continuum emission core but smaller than the Strömgren radius of the nebula.[18] The most distant CLASSY targets are LBAs at $z \approx 0.18$. Here, the COS aperture subtends nearly 8 kpc, vignetting extended halo emission but likely capturing most of the Lyα luminosity. CLASSY also includes several very nearby galaxies, where the COS aperture subtends just a few hundred parsecs, and the damped Lyα absorption troughs are prominent in their spectra (see Figures 1 and 2).

We suggest that the DLA detections indicate the Lyα emission is scattered outside the COS aperture. In support of this claim, Figure 6 shows that 14 of 16 galaxies with UV half-light radii larger than the COS aperture (Xu et al. 2022) have a DLA in their COS spectrum.[19] The frequency of DLA detections is reduced among the galaxies with half-light radii smaller than the COS aperture. The Lyman break analog sample has the fewest DLA detections. Although the physical size of the aperture grows with increasing redshift, we do not find a one-to-one correlation between DLA detections and redshift. For $z > 0.1$ (yellow circles), the physical scale of COS aperture reaches ∼5–10 kpc and is larger than the UV sizes of those galaxies; however, a large fraction (4/9) of their spectra still show significant DLA system. The spectra of high-redshift galaxies observed with similar aperture size sometimes show DLA systems as well (Steidel et al. 2011; Reddy et al. 2016, 2022; Lin et al. 2023). For example, Steidel et al. (2011) reveals a similar fraction (40/92) of galaxies at redshift ∼2.2–3.2, which shows the DLA system.

We can gain some quantitative insight from the Lyα imaging studies of Hayes et al. (2014). LARS 9 and LARS 14 correspond to the CLASSY galaxies J0823+2806 at $z = 0.04722$, and J0926+4427 at $z = 0.18067$, respectively.

[18] To estimate the volume ionized by the stars within the COS aperture we have used the extinction corrected the Hα luminosity in the SDSS fiber and assumed a volume-average electron density of 1 cm^{-3} and case B recombination at 10^4 K.

[19] The sizes of compact galaxies with $r_{50} < 0.''4$ are measured using COS acquisition images and the sizes of extended galaxies are measured using SDSS u-band images.

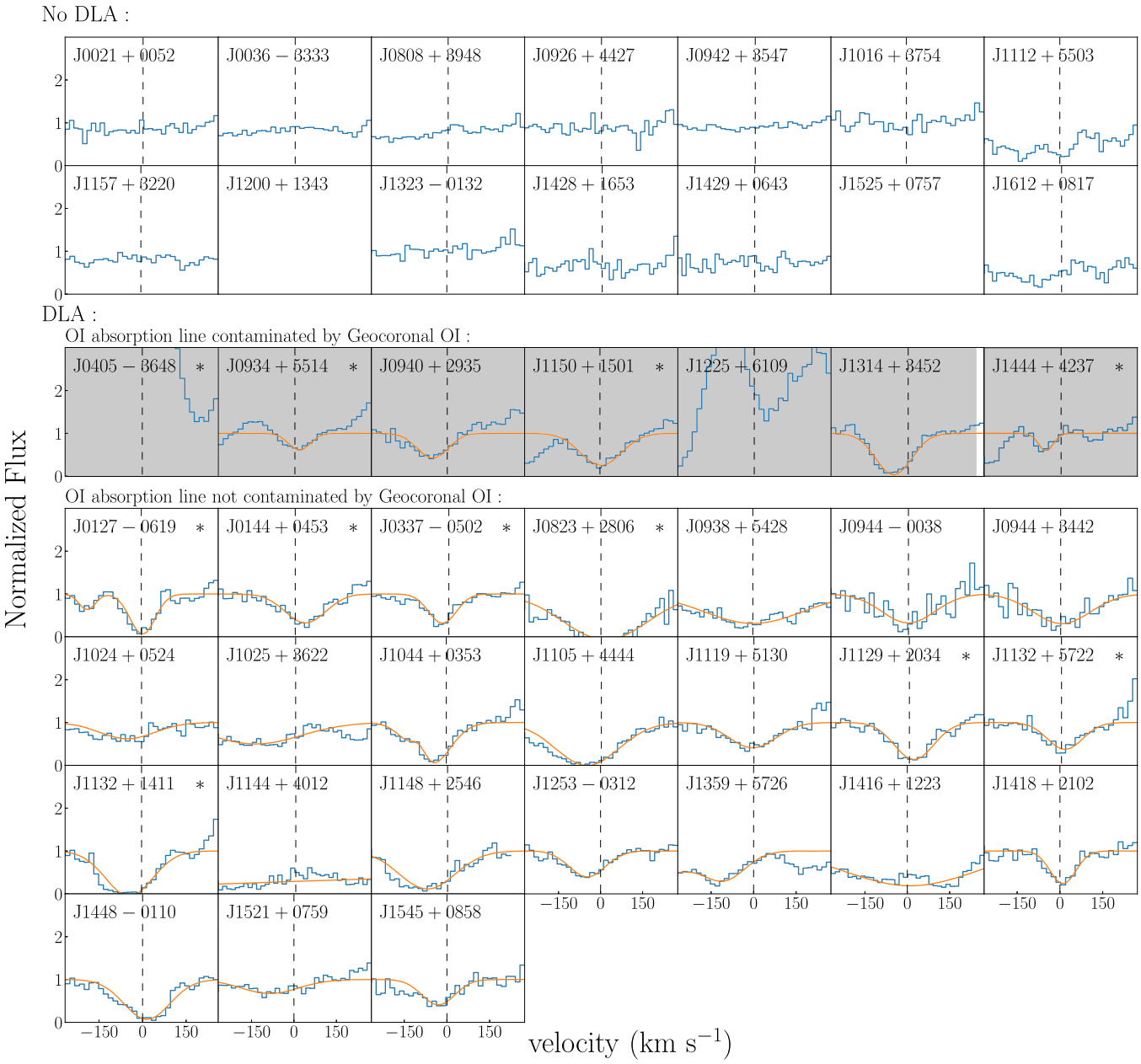

Figure 4. O I absorption profiles (blue) of CLASSY sample. The orange lines indicate best-fit Gaussian profiles. The first two rows show O I absorption profiles of galaxies without DLA system. The third row shows those O I profiles that might overlap with geocoronal O I emission, and the rest shows others. The shaded regions show the wavelength range (1302.2–1307.5 Å) that might be contaminated by geocoronal O I emission lines. An example of geocoronal O I line can be seen in the spectrum of J1525+0757, as shown in the online component of Figure 2. The O I absorption lines of 2 galaxies (J0405-3648 and J1225+6109) overlap with geocoronal O I line; thus, we adopt their C II velocities as DLA velocities. The vertical dashed lines indicate the zero velocity. Asterisks mark galaxies that show a pure DLA system with no Lyα emission.

The closer galaxy shows a pure-DLA Lyα profile, whereas the more distant one has a double-peaked emission profile with no DLA. An inspection of Figure 1 in Hayes et al. (2014) shows the Lyα emission comes from a shell around J0823+2806, whereas the Lyα emission from J0926+4427 is centrally concentrated. In the latter example, the COS aperture includes roughly 60% of the total Lyα flux (Hayes et al. 2014, Figure 4), showing that the Lyα luminosity is significantly attenuated even in the case of no absorption. For the DLA, the growth curve shows net emission only when the aperture is enlarged to a diameter of 9.5 kpc, about 4 times larger than the COS aperture. Galaxy-by-galaxy aperture corrections for Lyα are not currently available, but these examples support our conjecture that the galaxies showing damped Lyα absorption would show net emission in spectra obtained through larger apertures.

2.3. Lyα Measurements

In this section, we present the measurements of the Lyα emission properties. We measure the continuum and DLA-subtracted profiles. We will demonstrate in Section 3 that the Lyα emission emerges from holes between the DLA clouds. Since these parts of the line profile have different origins, they must be separated to obtain a meaningful analysis.

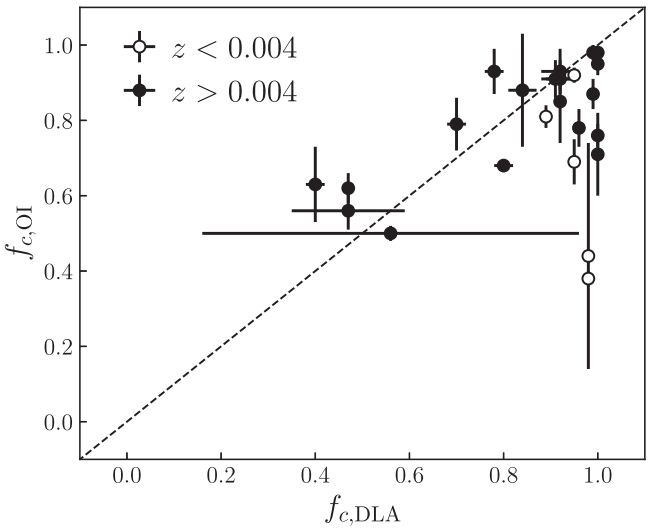

Figure 5. DLA covering fraction vs. O I covering fraction. We mark those O I covering fractions that are possibly contaminated by geocoronal O I emission line (at 1302.2–1307.5 Å) as open circles. Excluding those points, the observed correlation suggests O I covering fraction probe H I covering fraction.

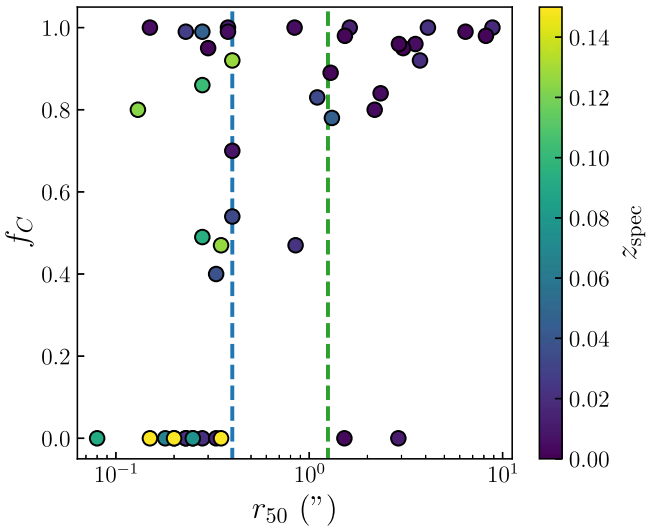

Figure 6. The DLA covering fraction vs. the angular UV half-light radius. A covering fraction of 0 indicates no DLA. We color-coded the circles based on their spectroscopic redshift, thereby identifying variations in the physical scale of the aperture. We also use the blue and green vertical dashed lines to indicate the unvignetted radius (0.″4) and the total radius (1.″25) for the COS aperture. Roughly a half of higher-redshift galaxies ($z > 0.1$) show significant DLA system. This fraction increases to the lower-redshift sample, which tends to have a larger UV size (in arcsec) due to the projection effect.

2.3.1. Lyα Kinematics

We measure the blue peak velocity, $v_{\mathrm{blue}}^{\mathrm{Ly}\alpha}$, and red peak velocity, $v_{\mathrm{red}}^{\mathrm{Ly}\alpha}$, as the position of the local maximum in the Lyα emission line at velocity $v < 0$ and $v > 0$, respectively, relative to the systemic velocity. The minimum between the two emission peaks defines the Lyα trough velocity, $v_{\mathrm{trough}}^{\mathrm{Ly}\alpha}$. We define the peak separation as $\Delta v_{\mathrm{Ly}\alpha} = v_{\mathrm{red}}^{\mathrm{Ly}\alpha} - v_{\mathrm{blue}}^{\mathrm{Ly}\alpha}$.

2.3.2. Lyα Fluxes and Lyα Escape Fraction

For double-peaked Lyα profiles, we measure the fluxes of the blue and red components by integrating to the velocity of the Lyα trough between the components. We also measure the asymmetry parameter of the red peak of Lyα emission, defined as $A_f = (\int_{\lambda_{\mathrm{peak}}^{\mathrm{red}}}^{\infty} f_\lambda\, d\lambda) \Big/ (\int_{\lambda_{\mathrm{trough}}}^{\lambda_{\mathrm{peak}}^{\mathrm{red}}} f_\lambda\, d\lambda)$, where $\lambda_{\mathrm{peak}}^{\mathrm{red}}$ is the wavelength of the red peak, and $\lambda_{\mathrm{trough}}$ is the wavelength of the trough (Rhoads et al. 2003; Kakiichi & Gronke 2021). The total Lyα fluxes are measured by integrating flux between the wavelengths where the profile meets zero flux, including the central dip in double-peaked profiles and the negative flux in P Cygni profiles. We convert the total Lyα fluxes to luminosity using the luminosity distance from Table 1, which is corrected for the cosmic flow. The rest-frame equivalent widths, EWs, are computed using the Lyα spectra and the *total stellar continuum*, $\mathrm{EW(Ly}\alpha) = \int F_{\mathrm{Ly}\alpha}(\lambda)/F_{\mathrm{cont}}(\lambda)\, d\lambda/(1+z)$.

We estimate the Lyα escape fractions $f_{\mathrm{esc}}^{\mathrm{Ly}\alpha}$ based on intrinsic Lyα fluxes inferred through dust-corrected Hα (or Hβ) fluxes assuming a Case B recombination (Brocklehurst 1971): $f_{\mathrm{esc}}^{\mathrm{Ly}\alpha} = F_{\mathrm{Ly}\alpha}/(8.7 \times F_{\mathrm{H}\alpha})$.[20] Mingozzi et al. (2022) have measured the Hα and Hβ fluxes using optical spectra from SDSS, MUSE, KCWI, MMT, and VIMOS. Since the UV spectra and optical spectra are obtained via different instruments with different aperture sizes, a scaling factor between UV spectra and optical spectra is needed to correct the different aperture losses. Mingozzi et al. (2022) measured the scaling factor by matching the optical spectra to the extrapolation of the best-fit UV stellar continuum model (see their Appendix A). The scaling factors for most objects approximate the ratio between apertures of different instruments but are not exactly the same because some other effects may also cause the flux offsets such as the vignetting. For example, the median of the scaling factor for SDSS spectra is ∼0.79, and the aperture size ratio is $(2.''5)^2/(3.''0)^2 \sim 0.69$. We refer readers to Mingozzi et al. (2022) for more details. In this work, we adopt the corrected Hα fluxes. Since the Hα for J0934+5514 and J1253-0312 are unavailable, we convert their Hβ fluxes to Hα fluxes using a factor of 2.86, by assuming Case B recombination with a temperature of 10,000 K and electron density of 100 cm^{-3}.

2.3.3. Lyα Trough Flux Density

The flux density at the Lyα trough velocity defines the trough flux density, f_{trough}. The f_{trough} of J0926+4427 and J1429+0643 have also been measured in Gazagnes et al. (2020) based on the spectra obtained by HST/COS G140L with a resolution of 1500. Gazagnes et al. (2020) measured the Lyα trough flux density based on the continuum-unsubtracted spectra, but our measurements are based on the continuum-subtracted Lyα spectrum. Thus, our $F_{\mathrm{trough}}/F_{\mathrm{cont}}$ should be lower by 1 compared to those in Gazagnes et al. (2020). Here, F_{cont} is the flux density of *total stellar continuum* estimated from STARBURST99.

However, accounting for this difference, the $F_{\mathrm{trough}}/F_{\mathrm{cont}}$ of J0926+4427 and J1429+0643 in our measurements are still lower. In particular, for J0926+4427, we do not see the net residual Lyα trough flux density (i.e., $F_{\mathrm{trough}} < 0$). This is because the CLASSY spectra have much higher resolution, ranging from ∼2200 to 15,000 with a median of 5000 (measured from MW absorption line; Berg et al. 2022). The high-resolution spectra resolve the small structures at the central trough, which were smoothed due to the lower resolution in Gazagnes et al. (2020). We note that the

[20] We adopt the factor of 8.7 to be consistent with previous works. It corresponds to a temperature of 10,000 K and an electron density of ∼300 cm^{-3}.

resolution around Lyα emission line might be lower than the resolution for the continuum as Lyα emission, which often subtends a larger solid angle than that of the continuum.

2.3.4. Aperture Effects on Lyα Measurements

The COS aperture, therefore, attenuates the Lyα emission relatively more than the UV emission due to the scattering of Lyα photons. Thus, even though Lyα Hα, and the UV continuum are measured locally in the same aperture, we expect $f_{\rm esc}^{\rm Ly\alpha}$ and the Lyα EW to be underestimated. In our example of J0823+2806, see discussion in Section 2.2, the attenuation is severe because most of the Lyα emission is scattered outside the COS aperture. If scattering outside the COS aperture produces the large fraction of DLA systems in CLASSY, then the $f_{\rm esc}^{\rm Ly\alpha}$ and Lyα EW of these galaxies are significantly underestimated.

A more subtle bias that we will examine is the possibility that this vignetting modifies the shape of the Lyα emission-line profile. Zheng et al. (2010) predicted that the blue-to-red peak ratio (hereafter B/R ratio) would increase with increasing impact parameters because the front-scattered Lyα photons (blue peak) are closer to the resonance center of the outflowing gas and, thus, tend to be scattered to larger impact parameters, compared with the back-scattered Lyα photons (red peak). Integral field spectroscopy confirms this trend in a few Lyα halos (Erb et al. 2018, 2023). Another possible interpretation is that the average projected outflow velocity decreases with the increasing radius (Li et al. 2022).

3. Radiative Transfer Modeling

The high fraction of DLA systems in CLASSY was not anticipated. More surprising, however, was the discovery of double-peaked Lyα emission in the bottom of the broad absorption profiles. We have drawn attention to an important property of these DLA systems; the high-column density gas only partially covers the continuum source (see Section 2.1). The residual intensity in the continuum-normalized spectra indicates the uncovered fraction of the continuum emission (within the COS aperture). In this section, we explore what continuum is linked to the net Lyα emission profile, the total continuum or the uncovered fraction.

Specifically, we utilize the shell model to fit the Lyα profiles that are normalized by the STARBURST99 continuum or the DLA continuum (hereafter normalized Lyα profile[21]). The model Lyα line profile is computed using the Monte Carlo radiative transfer code tlac (Gronke & Dijkstra 2014; Gronke et al. 2015). This technique has been used to successfully reproduce the observed profiles of Lyα emission lines (e.g., Yang et al. 2017; Orlitová et al. 2018; Gurung-López et al. 2022). The shell model can produce Lyα emission when the dust optical depth is low, or a DLA system when there is a substantial neutral hydrogen column with a moderate dust optical depth (e.g., see Figure 1 of Gronke et al. 2015). However, the homogeneous shell model cannot produce a Lyα emission line in the DLA trough, i.e., the Abs+Em profiles seen in our CLASSY sample (see Figure 2). The Lyα emission line requires low-$N_{\rm H\,I}$ channels (with low dust optical depth), which contradicts the presence of damped absorption, which requires very-high-column density. This requires a nonuniform shell model to describe the multicomponent ISM. Although radiative transfer through clumpy media has been explored (Hansen & Oh 2006; Verhamme et al. 2015; Gronke et al. 2016, 2017; Li & Gronke 2022), a nonuniform shell is beyond the scope of this work.

Here, we adopt an alternative method to fit the Lyα profiles of the CLASSY sample. We fit and remove the DLA system to extract the net Lyα profile, as described in Section 2.1, and then, we fit the tlac model to the normalized Lyα profile using two different approaches described in Section 3.2. The variant fitting results could reveal the physical links between the gasses probed by Lyα emission and DLA absorption, as discussed in Section 3.2.3.

Some properties of the shell model have been mapped to those of more realistic outflows (Gronke et al. 2016; Li & Gronke 2022). However, the shell-model parameters are found to have systematic discrepancies with independently measured outflow velocities and the velocity dispersion of the intrinsic line profile (e.g., Orlitová et al. 2018). To understand the origin of the discrepancies, we perform more fittings with constrained redshift priors and compare it with the previous results in Section 3.3.

3.1. Shell Model

tlac computes Lyα resonant scattering through a uniform, expanding shell, which is composed of dust and neutral hydrogen gas. The shell model used in tlac has 6 free parameters, including 2 parameters for the central radiation source: intrinsic line width σ_i and intrinsic equivalent width EW$_i$; and 4 parameters for the expanding shell (neutral hydrogen column density $N_{\rm H\,I}$, dust optical depth $\tau_{\rm d}$, shell velocity $v_{\rm exp}$, and temperature T). In addition to these six parameters, a redshift parameter $z_{\rm tlac}$ is also applied to shift the rest frame of the Lyα profile relative to the systemic redshift of the galaxy.

The Lyα photons and underlying continuum photons are generated from the central source with an intrinsic width of σ_i and intrinsic equivalent width of EW$_i$. The photon is then emitted into the H I shell with a random direction and travels a distance before being absorbed or resonantly scattered. The distance that a photon can travel is calculated using the total optical depth of dust $\tau_{\rm d}$ and neutral hydrogen $N_{\rm H\,I}$ in the expanding shell with velocity $v_{\rm exp}$ and temperature T. The probability that a photon is resonantly scattered or absorbed at a specific position is estimated by comparing the optical depth of neutral hydrogen with the total optical depth at that position. If the photon is resonantly scattered, a new direction and a new frequency are drawn from the proper phase function and the frequency redistribution function, respectively. The previous steps are repeated until the photon escapes from the simulation domain or is absorbed by the dust. If the photons escape from the simulation domain, their frequency, and other properties are recorded. This simulation has been run thousands of times over a discrete grid of ($v_{\rm exp}$, $N_{\rm H\,I}$, T) and then been post-processed with a continuous grid of (σ_i, $\tau_{\rm d}$, EW$_i$) to generate the simulated Lyα spectra for different parameter values. To fit the observed Lyα spectrum, a likelihood function is constructed based on the noise and flux spectra. The best-fit spectrum is derived by maximizing the likelihood function using the

[21] To avoid confusion, we define the emergent Lyα profile as the observed Lyα emission line with the underlying continuum and DLA, the net Lyα profile as the Lyα profile after removing the underlying continuum and DLA, and the normalized Lyα profile as the net Lyα profile after being normalized by the underlying continuum.

Markov Chain Monte Carlo and nonlinear optimization methods.

We highlight the importance of the intrinsic Lyα equivalent width (EW_i) in the shell model, a parameter excluded by studies that fit the continuum-subtracted Lyα line profiles, because the continuum photons are also involved in resonant scattering and can dominate the normalized Lyα profile for low-EW_i cases.

3.2. Profile Fitting

Our profile-fitting approach draws attention to ambiguity about the appropriate continuum level for normalization. When a DLA system is present in the spectrum, the underlying continuum could be the total stellar continuum (red lines in panel (a) of Figure 2), and thus, the normalized spectrum is as follows:

$$I_\lambda^{\rm EW} = (f_\lambda^{\rm Ly\alpha} + f_\lambda^{\rm cont})/(f_\lambda^{\rm cont}), \quad (3)$$

or the residual stellar continuum in the bottom of DLA system (red line in panel (b)). And thus, the normalized spectrum is as follows:

$$I_\lambda^{\rm EW} = (f_\lambda^{\rm Ly\alpha} + f_\lambda^{\rm cont} \times (1 - f_C))/(f_\lambda^{\rm cont} \times (1 - f_C)), \quad (4)$$

where $f_\lambda^{\rm Ly\alpha}$ is the Lyα emission line, $f_\lambda^{\rm cont}$ is the best-fit total stellar continuum (see Section 2), and f_C is the covering fraction of DLA system. The choice of the underlying continuum will change the equivalent width of the Lyα line and, thus, the contribution of continuum photons on the emergent Lyα profile. Here, we perform profile fittings, assuming each continuum level in turn, and then discuss the results. We present the best-fit spectra in Appendix. We also present the best-fit model parameters of the second profile fitting in Table 4.

The fitted parameters somewhat degenerate with each other. For example, in the case of outflowing shells, Li & Gronke (2022) demonstrate that various combinations of shell velocity, column density, temperature, and redshift can produce very similar line profiles, for example, ($v_{\rm exp}$, $\log N_{\rm H\,I}$, $\log T$, 0), and $\sim$($2v_{\rm exp}$, $\log N_{\rm H\,I} - 0.5$ dex, $\log T + 1$ dex, Δv). Nonetheless, the spectra generated by these parameters show clear differences at the red peak, and our high-S/N spectra should be able to distinguish between the degeneracies.

3.2.1. First Attempt: Total Stellar Continuum

Overall, the quality of the first fitting using the total stellar continuum (Equation (3)) is quite good, given the simplicity of the model. However, in a subset of spectra, the results are unsatisfactory, especially J0938+5428, J0944+3442, J1044+0353, J1119+5130, J1144+4012, J1416+1223, J1521+0759, as presented in Figure 18, of which the best-fit spectra show a very sharp dip around zero velocity compared to the observed Lyα profile.

Looking at their original spectra (see Figure 2), we find that all these poorly fitted Lyα profiles correspond to spectra that show significant DLA systems compared with the successful sample. This result motivated us to investigate whether the sharp dips might be caused by an inappropriate underlying continuum, which underestimated the Lyα EW spectra $I_\lambda^{\rm EW}$. Thus, we performed a second profile fitting using the residual stellar continuum as described by Equation (4).

3.2.2. Second Attempt: Residual Stellar Continuum

In Figure 19, we present the best-fit tlac models for Lyα profiles normalized by the residual stellar continua ($1 - f_C$). For the unsatisfactory sample in the first attempt, normalizing the Lyα spectra by the residual stellar continuum significantly improved the best-fit results. The sharp dips seen in the models of Section 3.2.1 no longer exist in the new model spectra. In Figure 7, we compare the reduced χ^2 for the first and second attempts. Clearly, most results are significantly improved if adopting the normalization of the residual stellar continuum. Thus, we can conclude that the dip was caused by an inappropriate continuum level. In further analysis, the first attempt of fitting will not be considered.

For the galaxies without DLA systems, $f_C = 0$, the residual continuum rises to the level of the total continuum. It is therefore not surprising that every Lyα profile is successfully fitted when the residual continuum is used. We conclude that the residual continuum, $1 - f_C$, is the more physical normalization for the emergent Lyα emission line. In other words, the DLA covering fraction f_C gives a good indication of the fraction of the intrinsic Lyα emission that is blocked by the high-column density clouds.

3.2.3. Implication: Scattering Outside COS Aperture Reveals Low-$N_{H\,I}$ Channels

We have shown that successful radiative transfer modeling of CLASSY Lyα spectra, in the context of the shell model, requires (1) separating the Lyα emission profile from the DLA system, and (2) normalizing the Lyα emission by the leaked continuum, i.e., the residual flux in the DLA system. This approach divides the COS aperture into two groups of sightlines, hereafter channels, distinguished by their column density. In the schematic picture of a thin shell, these two channels represent clouds and the intercloud medium. More generally, for the targets with $C_f > 0$, the Lyα photons entering the high-$N_{\rm H\,I}$ channel do not emerge from the galaxy at radii within the COS aperture. If they did, then the best continuum normalization would be the total stellar continuum, which is inconsistent with our fitting results.

The Lyα photons entering the high-$N_{\rm H\,I}$ channel must be scattered to radii larger than the COS aperture before they escape. The alternative is that they are absorbed by dust grains, which seems less likely for two reasons. Most CLASSY galaxies whose COS spectra detect DLA systems have low metallicities and are relatively dust poor. In addition, substantial amounts of dust in the scattering clouds would boost the transmitted Lyα equivalent width (Hansen & Oh 2006), but we do not measure unusually large EW.

When the Lyα emission is separated from the DLA system, what do the shell-model parameters fitted to the emission component represent? Perhaps, the line photons entering low-$N_{\rm H\,I}$ channels scatter off both the low $N_{\rm H\,I}$ clouds and the walls of the DLA channels. In the limit of no intercloud medium, the kinematics of the dense clouds would determine the shape of the Lyα line profile (Neufeld 1990; Hansen & Oh 2006), so we might expect the kinematics of both the low- and high-$N_{\rm H\,I}$ channels to impact the Lyα profile. If Lyα photons entering DLA sightlines are scattered outside the spectroscopic aperture, then the vignetted apertures may have one advantage, namely providing a direct view of the properties in low-$N_{\rm H\,I}$ channels.

Table 4
Best-fit Parameters of the Second Attempt

Object	$z_{\rm tlac}$	$v_{\rm exp}$ (km s^{-1})	log $N_{\rm H\,I}$	log T (K)	log τ	σ_i (km s^{-1})	EW$_i$ (Å)
(1)	(2)	(3)	(4)	(5)	(6)	(7)	(8)
J0021+0052	0.098902	214^{+1}_{-2}	$18.79^{+0.11}_{-0.08}$	$3.8^{+0.2}_{-0.1}$	$-2.05^{+1.01}_{-0.11}$	117^{+1}_{-1}	$16.8^{+0.8}_{-0.7}$
J0036-3333	0.020939	207^{+2}_{-1}	$18.68^{+0.09}_{-0.06}$	$3.5^{+0.2}_{-0.1}$	$-2.10^{+1.13}_{-0.06}$	93^{+1}_{-1}	$6.6^{+0.5}_{-0.1}$
J0808+3948	0.091384	365^{+1}_{-1}	$16.76^{+0.08}_{-0.04}$	$3.4^{+0.1}_{-0.1}$	$-1.57^{+0.22}_{-0.11}$	103^{+1}_{-1}	$8.7^{+0.1}_{-0.1}$
J0926+4427	0.180817	131^{+2}_{-3}	$19.23^{+0.05}_{-0.08}$	$3.7^{+0.1}_{-0.1}$	$-1.74^{+0.11}_{-0.21}$	248^{+2}_{-3}	$31.8^{+1.0}_{-1.0}$
J0938+5428	0.102513	21^{+4}_{-2}	$19.79^{+0.08}_{-0.08}$	$4.2^{+0.2}_{-0.1}$	$-0.68^{+0.74}_{-0.87}$	308^{+5}_{-4}	$74.5^{+5.3}_{-4.4}$
J0942+3547	0.015121	86^{+1}_{-1}	$18.20^{+0.06}_{-0.06}$	$3.1^{+0.1}_{-0.1}$	$-3.31^{+0.38}_{-0.09}$	167^{+1}_{-1}	$18.3^{+0.1}_{-0.1}$
J0944-0038	0.005187	119^{+4}_{-4}	$18.60^{+0.09}_{-0.07}$	$3.4^{+0.2}_{-0.2}$	$-1.35^{+0.20}_{-0.12}$	218^{+3}_{-4}	$2130.2^{+1851.2}_{-1159.2}$
J0944+3442	0.020226	72^{+18}_{-17}	$19.44^{+0.21}_{-0.23}$	$4.1^{+0.7}_{-0.8}$	$0.44^{+0.46}_{-0.43}$	182^{+12}_{-11}	$39.6^{+21.4}_{-14.0}$
J1016+3754	0.004131	96^{+2}_{-1}	$18.85^{+0.07}_{-0.11}$	$4.3^{+0.1}_{-0.2}$	$0.10^{+0.80}_{-0.75}$	142^{+1}_{-2}	$26.2^{+1.9}_{-1.9}$
J1024+0524	0.033425	176^{+2}_{-1}	$19.01^{+0.08}_{-0.09}$	$5.1^{+0.1}_{-0.2}$	$-1.89^{+0.92}_{-0.16}$	82^{+1}_{-1}	$16.2^{+0.6}_{-0.4}$
J1025+3622	0.126786	167^{+3}_{-2}	$18.99^{+0.09}_{-0.07}$	$4.2^{+0.2}_{-0.1}$	$-0.88^{+0.40}_{-0.55}$	245^{+3}_{-3}	$41.3^{+2.1}_{-1.9}$
J1044+0353	0.013070	175^{+10}_{-15}	$18.18^{+0.20}_{-0.19}$	$3.5^{+0.3}_{-0.4}$	$-1.14^{+0.25}_{-0.10}$	248^{+14}_{-9}	$9.9^{+0.9}_{-0.7}$
J1112+5503	0.131707	210^{+3}_{-3}	$19.55^{+0.10}_{-0.05}$	$4.6^{+0.3}_{-0.1}$	$0.55^{+1.10}_{-1.17}$	270^{+3}_{-4}	$20.9^{+1.5}_{-1.6}$
J1119+5130	0.004536	0^{+2}_{-1}	$20.42^{+0.24}_{-0.65}$	$4.0^{+0.4}_{-0.3}$	$-1.80^{+1.21}_{-0.03}$	316^{+10}_{-8}	$6.5^{+6.6}_{-2.4}$
J1144+4012	0.126832	108^{+11}_{-8}	$20.20^{+0.07}_{-0.08}$	$4.9^{+0.3}_{-0.7}$	$0.40^{+0.46}_{-0.52}$	259^{+9}_{-11}	$281.6^{+50.7}_{-41.7}$
J1148+2546	0.045710	279^{+5}_{-4}	$19.19^{+0.09}_{-0.07}$	$3.8^{+0.2}_{-0.2}$	$0.53^{+0.67}_{-0.56}$	281^{+4}_{-4}	$46.3^{+3.7}_{-3.6}$
J1157+3220	0.010230	163^{+1}_{-2}	$20.06^{+0.04}_{-0.09}$	$5.0^{+0.1}_{-0.2}$	$0.69^{+1.98}_{-1.60}$	191^{+1}_{-2}	$200.1^{+2.7}_{-3.5}$
J1200+1343	0.066942	173^{+1}_{-2}	$16.56^{+0.09}_{-0.05}$	$5.4^{+0.1}_{-0.1}$	$-2.40^{+0.65}_{-0.12}$	266^{+1}_{-1}	$53.6^{+1.7}_{-1.8}$
J1253-0312	0.023087	184^{+0}_{-1}	$18.67^{+0.03}_{-0.06}$	$4.3^{+0.1}_{-0.1}$	$-2.70^{+0.48}_{-0.00}$	256^{+1}_{-1}	$31.2^{+0.5}_{-0.4}$
J1323-0132	0.022534	37^{+1}_{-1}	$17.93^{+0.05}_{-0.02}$	$3.1^{+0.0}_{-0.1}$	$-2.40^{+0.24}_{-0.12}$	121^{+0}_{-0}	$75.7^{+1.1}_{-1.1}$
J1359+5726	0.034107	205^{+2}_{-1}	$19.03^{+0.13}_{-0.09}$	$4.7^{+0.1}_{-0.2}$	$-1.11^{+0.10}_{-0.47}$	128^{+2}_{-2}	$51.8^{+2.5}_{-2.2}$
J1416+1223	0.123181	0^{+2}_{-2}	$19.59^{+0.09}_{-0.08}$	$4.6^{+0.2}_{-0.3}$	$-0.22^{+0.70}_{-0.73}$	289^{+6}_{-6}	$49.5^{+4.1}_{-3.9}$
J1418+2102	0.009016	98^{+2}_{-2}	$18.18^{+0.09}_{-0.06}$	$3.0^{+0.1}_{-0.1}$	$0.68^{+1.65}_{-1.61}$	230^{+1}_{-1}	$101.8^{+4.8}_{-4.9}$
J1428+1653	0.181780	121^{+3}_{-4}	$18.80^{+0.10}_{-0.07}$	$3.5^{+0.1}_{-0.2}$	$-1.12^{+0.08}_{-0.40}$	52^{+1}_{-1}	$17.8^{+1.9}_{-1.0}$
J1429+0643	0.173984	112^{+2}_{-3}	$19.21^{+0.08}_{-0.09}$	$3.1^{+0.2}_{-0.2}$	$-0.38^{+0.67}_{-0.82}$	323^{+5}_{-5}	$46.8^{+3.6}_{-3.1}$
J1521+0759	0.094771	215^{+2}_{-2}	$19.08^{+0.12}_{-0.11}$	$3.0^{+0.2}_{-0.1}$	$-1.04^{+0.16}_{-0.28}$	93^{+2}_{-2}	$9.2^{+1.8}_{-0.6}$
J1525+0757	0.075913	136^{+2}_{-1}	$18.58^{+0.09}_{-0.06}$	$4.5^{+0.2}_{-0.1}$	$-1.39^{+0.00}_{-0.44}$	52^{+1}_{-1}	$19.2^{+1.2}_{-1.0}$
J1545+0858	0.038336	194^{+1}_{-2}	$18.41^{+0.07}_{-0.10}$	$3.0^{+0.2}_{-0.1}$	$0.69^{+1.91}_{-1.58}$	156^{+1}_{-1}	$55.3^{+1.5}_{-1.8}$
J1612+0817	0.149267	246^{+3}_{-2}	$19.61^{+0.08}_{-0.10}$	$5.3^{+0.2}_{-0.2}$	$0.09^{+1.03}_{-1.11}$	112^{+2}_{-2}	$35.6^{+2.3}_{-2.0}$

Note. (1) Object name; (2) redshift estimated by the shell model; (3) outflow velocity of expanding shell; (4) H I column density; (5) temperature; (6) dust extinction; (7) intrinsic line width; (8) equivalent width.

(This table is available in machine-readable form.)

3.3. Discrepancies between the Shell Model and Observations

We have presented that whether the shell model can well-fit the observed Lyα profile is critical to infer the ISM properties. However, the three discrepancies reported in Orlitová et al. (2018; see also Section 1) might suggest a limited physical meaning of the model parameters. These discrepancies are also observed in the CLASSY sample with high significance, as shown in Figure 8 (black circles). The best-fit redshifts are always larger by 0–200 km s^{-1} than the spectroscopic redshift, consistent with Orlitová et al. (2018). One possible origin of the discrepancies is the degeneracies between the model parameters, suggested in Li & Gronke (2022). To test this scenario and gain more insight into the discrepancies, we perform a third profile fitting following Li & Gronke (2022), which constrains the range of redshift parameters to break the degeneracies.

3.3.1. Third Attempt: Constraining the Redshift

The CLASSY redshifts derived from UV nebular lines agree well with those derived from optical lines; the standard deviation of velocity difference is $\sim$22 km s^{-1} (Mingozzi et al. 2022). A spatial offset between the scattered Lyα emission and the optically thin emission lines would introduce an additional redshift error if, and only if, the offset were along the dispersion axis of the spectrograph. Based on the radius of the unvignetted aperture (0.″4), a nonperfect alignment could shift the Lyα wavelength scale by as much as $\pm$44 km s^{-1}. For a redshift-constrained fit, we adopted a narrow Tophat probability distribution of width $\pm$44 km s^{-1} as the prior on redshift. The best-fit spectra are presented in Figure 9. In contrast, in the second attempt at profile fitting (Section 3.2.2), we adopted a Gaussian prior on redshift, and this broad distribution with $\sigma(z_{\rm tlac}) = 120$ km s^{-1} serves as the unconstrained fit.

3.3.2. Can Constrained Fitting Alleviate the Discrepancies?

The redshift differences are apparently improved when adopting the constrained fitting (red circles in Figure 8). This is because the constrained redshift prior sets a hard limit of the difference to be 44 km s^{-1}. On the other hand, comparing the best-fit Lyα profiles of the constrained fitting (see Figure 9) with those of the unconstrained fitting (see Figure 19), it is hard

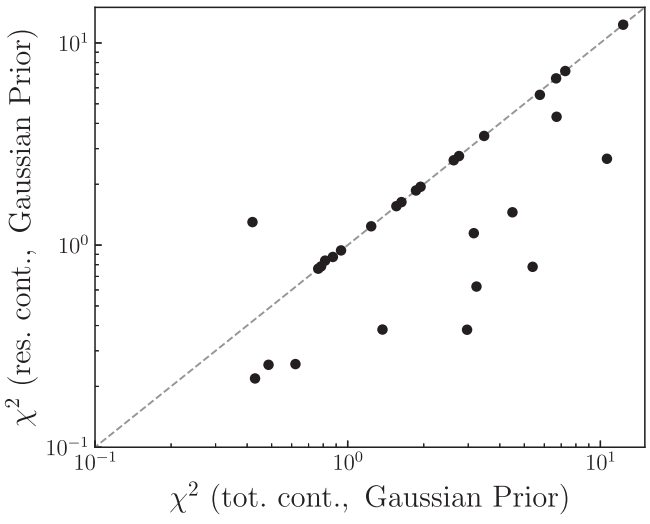

Figure 7. Reduced χ^2 values of best-fit Lyα profiles derived by the first attempt of profile fitting (using total stellar continuum and Gaussian redshift prior) and the second attempt of profile fitting (using residual stellar continuum and Gaussian redshift prior). We notice that, except for one object (J0944-0038), the fitting results for objects with DLA are significantly improved if adopting the residual continua, which are corrected for the DLA covering fraction $(1 - f_c)$. For objects without DLA, the corrected continuum equals to the total stellar continuum. Thus, the reduced χ^2 does not change. We note the reduced χ^2 of some galaxies (J0944+3442, J1044+0353, J1144+4012, J1148+2546, J1416+1223) are much smaller than unity. This might be due to their error spectra being overestimated (comparing to their flux fluctuation, see Figure 3).

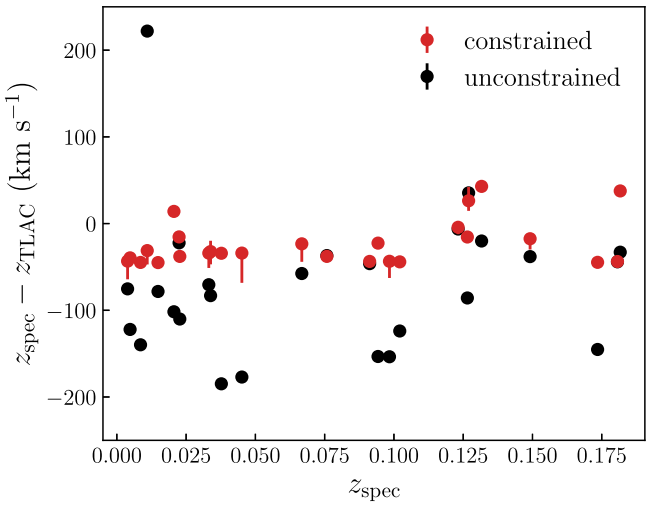

Figure 8. Redshift difference between tlac redshift $z_{\rm tlac}$ and spectroscopic redshift $z_{\rm spec}$. The black circles indicate the results of the second attempt of profile fitting with a Gaussian prior with $\sigma = 120$ km s^{-1} for redshift (unconstrained fitting). The red circles indicate the results of the third attempt of profile fitting with a Tophat prior with a width of ± 44 km s^{-1} for redshift (constrained fitting).

to distinguish the difference between them by visual inspection. We compare the reduced χ^2 of two profile fittings in Figure 10, which shows that the results of constrained profile fitting are slightly worse than those of unconstrained profile fitting, but still acceptable.[22] Thus, our test confirms that adopting a constrained redshift prior for the profile fitting can somewhat alleviate the redshift discrepancy observed in previous works (Yang et al. 2016; Orlitová et al. 2018). We present the best-fit parameters of the third profile fitting in Table 5.

However, the best-fit redshift remains systematically larger than the spectroscopic redshift as most of the red circles are still below zero velocity. This indicates that the constrained fitting does not fully resolve the observed discrepancies. We return to this topic in Section 4.3.3, where we combine the comparison between the tlac shell velocity and spectral measurements of outflow velocity.

We do not discuss the line width discrepancy in this work because a clumpy model is needed to resolve this discrepancy. By comparing the Lyα profiles generated by the uniform shell model and a clumpy model, Gronke et al. (2017), Li & Gronke (2022) find that a larger line width is always required for the shell model to produce a similar Lyα profile as that from the clumpy model. The intrinsic difference between the two models is that the clumpy model includes the turbulent velocity dispersion of the clumps while the shell model does not. Thus, the line width of the shell model needs to be artificially broadened to compensate for the omission of turbulent motion in the shell model.

4. Properties of the Neutral ISM

In this section, we discuss the relationship between the H I column densities inferred from the Lyα absorption and emission components of the line profile. We then discuss indirect evidence LyC leakage. Finally, we return to the problem of why the shell model systematically mispresents outflow properties, finding that the problem lies in the spectroscopic aperture.

4.1. Structure of the ISM in CLASSY Galaxies

In Section 3, we found evidence that the neutral ISM consists of several components with different column densities. The DLA system requires high-$N_{\rm H\,I}$ clouds with $N_{\rm H\,I} > 10^{20}$ cm^{-2}. In Section 3.2, the tlac fitting revealed that the observed Lyα emission line requires low-$N_{\rm H\,I}$ holes with $10^{18} < N_{\rm H\,I} < 10^{20}$ cm^{-2}. Combining these two results demonstrates the existence of sightlines with different H I column densities in individual galaxies. We have argued that the scattering of a significant fraction of the Lyα photons out of the COS aperture makes the high-$N_{\rm H\,I}$ channels visible via Lyα absorption, whereas their damping profiles would be filled in by scattered emission in spectra obtained through larger apertures. Apparently, the Lyα halos of many CLASSY galaxies are much larger than the COS aperture, and the scattering of Lyα photons out of the COS aperture provides a unique opportunity to describe the structure of the neutral ISM, as we show here.

New insight into how LyC radiation escapes from local analogs of EoR galaxies may be obtained by comparing the structure of the ISM in hydrodynamical simulations to the column density distribution we derive. Feedback from massive stars is widely believed to shape the pathways for LyC escape, but the mechanism is debated. For example, Ma et al. (2020) argue that positive feedback, essentially propagating star formation triggered by the mechanical feedback from massive stars, is essential to shift the production of LyC radiation away from the densest region of a galaxy. In contrast, in H II regions too young to have produced supernova explosions, the

[22] We notice two best-fit spectra (J1112+5503, J1323-0132) of constrained profile fitting are improved compared with the unconstrained profile fitting. This might be because the unconstrained profile fitting for these two objects is trapped in a local maximum of the likelihood.

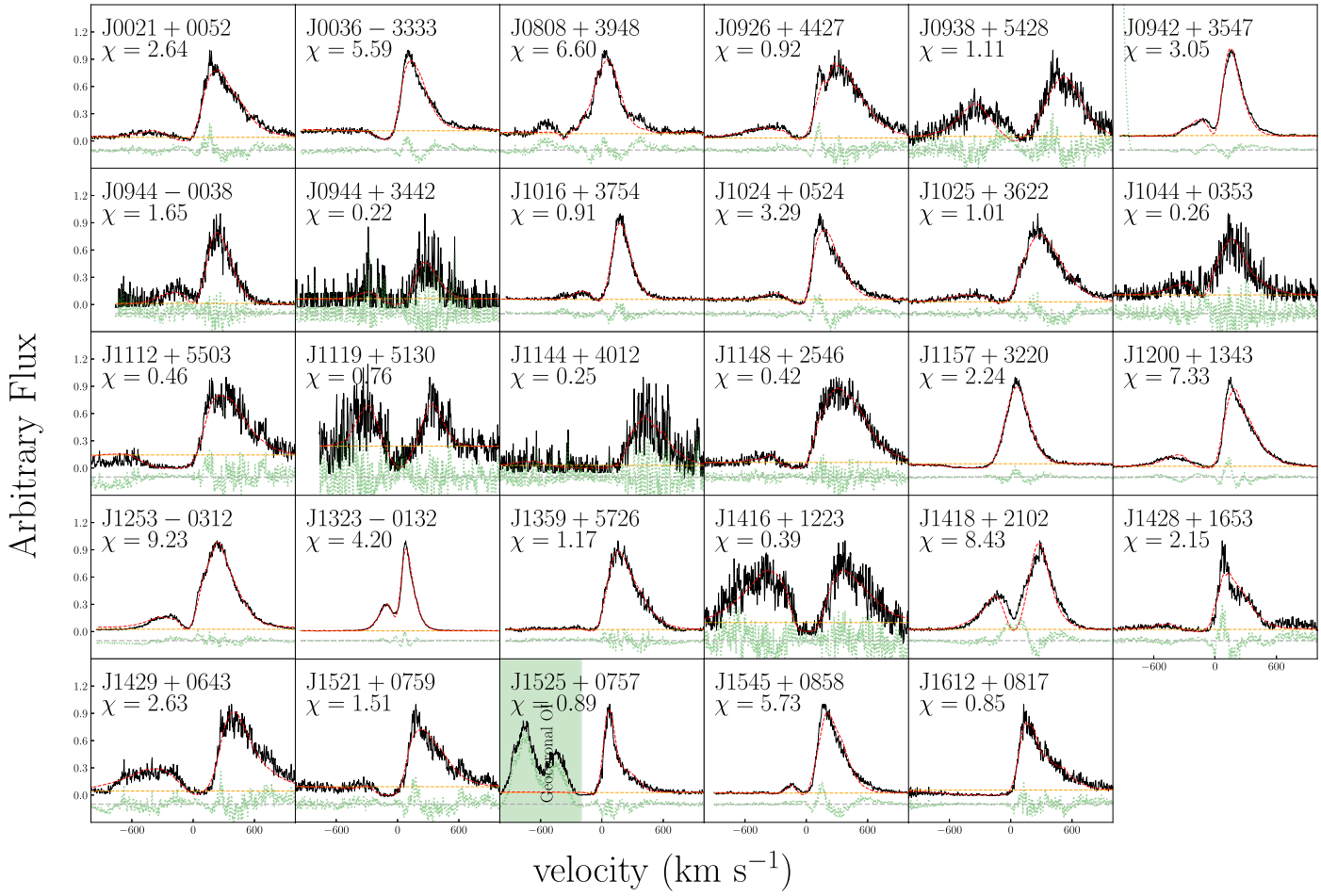

Figure 9. Best-fit Lyα spectra (red) for 29 CLASSY galaxies using the residual stellar continuum and a Tophat redshift prior with a width of ± 48 km s^{-1} (third attempt). The spectra are normalized by the peak flux, and the orange dashed lines indicate the continuum level for each object. We use the green lines to show the residual and manually shift it by -0.1 for better illustration. The gray dashed lines indicate the zero level of the residual.

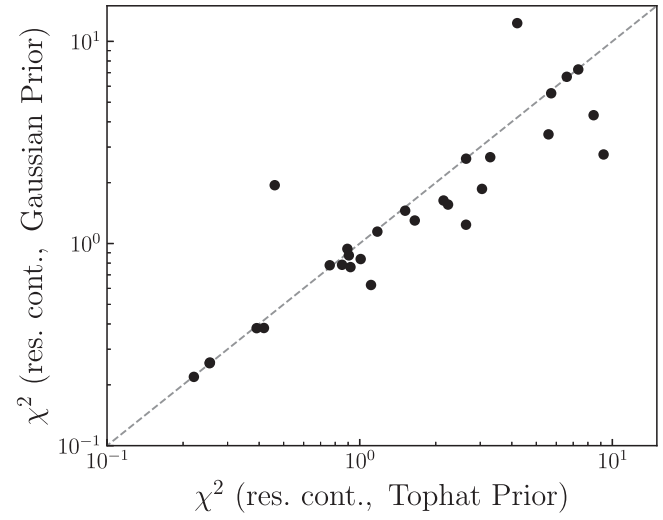

Figure 10. Reduced χ^2 values of best-fit Lyα profiles derived by the second attempt (using the residual continuum and a Gaussian redshift prior) and the third attempt (using the residual continuum and a Tophat redshift prior). The second attempt adopts a Gaussian probability distribution with σ of 120 km s^{-1} as prior, and the third attempt adopts a Tophat probability distribution with a width of ± 48 km s^{-1} as prior.

turbulence driven by ionization fronts may open channels for LyC escape (Kakiichi & Gronke 2021).

One difference between these two mechanisms is the size of the channels. Whereas the channels opened by turbulence are individually small, the low-$N_{\rm H\,I}$ bubbles driven by mechanical feedback have scales reaching hundreds of parsecs (Ma et al. 2020). Thus, the size of the channels provides insight of particular interest for understanding the escape pathways.

In this section, we adopt the column density estimation from the third profile fitting (see Section 3.3), because it incorporates more constraints from the observation. However, adopting the estimation from the second profile fitting does not change the conclusion of this section.

4.1.1. Column Density Distribution of Neutral ISM

Figure 11 compares the distribution of low-$N_{\rm H\,I}$ channels returned by the shell-model fits and the high-$N_{\rm H\,I}$ column densities measured from the damping wing absorption. In the top panel, the histograms are normalized by the total number of galaxies showing a DLA system or Lyα emission line, respectively. Their combined distribution has two peaks: one at $N_{\rm H\,I} \approx 10^{19}$ cm^{-2}, which represents the path of the escaping Lyα photons,[23] and a second peak representing the typical

[23] If adopting the $N_{\rm H\,I}$ from the second profile fitting, the peak shifts to lower by 0.4 dex.

Table 5
Best-fit Parameters of the Third Attempt

Object	$z_{\rm tlac}$	$v_{\rm exp}$ (km s^{-1})	log $N_{\rm H\,I}$	log T (K)	log τ	σ_i (km s^{-1})	EW$_i$ (Å)
(1)	(2)	(3)	(4)	(5)	(6)	(7)	(8)
J0021+0052	0.098535	163^{+1}_{-2}	$19.17^{+0.16}_{-0.05}$	$4.5^{+0.2}_{-0.1}$	$-0.67^{+0.19}_{-0.07}$	225^{+1}_{-1}	$26.7^{+4.0}_{-1.1}$
J0036-3333	0.020553	120^{+2}_{-2}	$19.17^{+0.08}_{-0.05}$	$3.0^{+0.1}_{-0.1}$	$-0.63^{+0.04}_{-0.04}$	142^{+2}_{-2}	$9.0^{+0.3}_{-0.3}$
J0808+3948	0.091375	348^{+2}_{-2}	$16.17^{+0.08}_{-0.05}$	$3.7^{+0.1}_{-0.1}$	$-1.67^{+0.46}_{-0.73}$	102^{+1}_{-1}	$8.7^{+0.1}_{-0.1}$
J0926+4427	0.180816	133^{+1}_{-1}	$19.19^{+0.07}_{-0.06}$	$3.8^{+0.1}_{-0.2}$	$-1.73^{+0.24}_{-0.38}$	244^{+3}_{-3}	$29.9^{+1.3}_{-1.2}$
J0938+5428	0.102247	11^{+1}_{-2}	$20.63^{+0.05}_{-0.11}$	$4.3^{+0.1}_{-0.2}$	$-2.44^{+0.45}_{-0.56}$	291^{+5}_{-4}	$31.8^{+3.9}_{-1.7}$
J0942+3547	0.015010	69^{+0}_{-0}	$18.58^{+0.03}_{-0.03}$	$3.3^{+0.0}_{-0.0}$	$-3.67^{+0.58}_{-0.73}$	170^{+1}_{-1}	$18.4^{+0.2}_{-0.2}$
J0944-0038	0.004912	70^{+3}_{-3}	$19.42^{+0.06}_{-0.08}$	$3.9^{+0.3}_{-0.2}$	$-2.21^{+0.54}_{-0.71}$	217^{+3}_{-4}	$302.0^{+23.0}_{-24.3}$
J0944+3442	0.020138	59^{+9}_{-10}	$19.61^{+0.11}_{-0.10}$	$3.3^{+0.9}_{-0.4}$	$0.34^{+0.23}_{-0.35}$	179^{+11}_{-11}	$55.8^{+18.3}_{-18.1}$
J1016+3754	0.004024	81^{+2}_{-2}	$19.04^{+0.13}_{-0.11}$	$3.8^{+0.3}_{-0.1}$	$-0.58^{+0.09}_{-0.08}$	148^{+2}_{-1}	$21.6^{+2.4}_{-1.3}$
J1024+0524	0.033304	139^{+3}_{-3}	$19.05^{+0.12}_{-0.11}$	$4.6^{+0.1}_{-0.1}$	$-0.69^{+0.14}_{-0.08}$	192^{+2}_{-2}	$20.0^{+2.5}_{-0.8}$
J1025+3622	0.126552	131^{+2}_{-4}	$19.43^{+0.07}_{-0.08}$	$3.9^{+0.3}_{-0.2}$	$-1.31^{+0.34}_{-0.35}$	243^{+3}_{-3}	$38.2^{+3.6}_{-2.3}$
J1044+0353	0.012998	158^{+9}_{-9}	$18.40^{+0.11}_{-0.13}$	$3.4^{+0.3}_{-0.3}$	$-1.16^{+0.44}_{-0.63}$	253^{+12}_{-8}	$9.9^{+0.9}_{-0.8}$
J1112+5503	0.131497	153^{+3}_{-4}	$19.83^{+0.06}_{-0.09}$	$3.8^{+0.2}_{-0.2}$	$0.25^{+0.08}_{-0.07}$	257^{+4}_{-4}	$26.8^{+2.7}_{-2.4}$
J1119+5130	0.004532	1^{+1}_{-2}	$20.18^{+0.10}_{-0.12}$	$4.6^{+0.1}_{-0.2}$	$-0.91^{+0.31}_{-0.26}$	225^{+9}_{-9}	$13.2^{+6.2}_{-4.6}$
J1144+4012	0.126862	111^{+12}_{-7}	$20.19^{+0.08}_{-0.07}$	$4.8^{+0.3}_{-1.0}$	$0.48^{+0.13}_{-0.19}$	252^{+8}_{-10}	$324.8^{+52.3}_{-63.3}$
J1148+2546	0.045233	187^{+6}_{-5}	$19.66^{+0.15}_{-0.11}$	$5.0^{+0.1}_{-0.2}$	$-1.50^{+0.58}_{-0.60}$	265^{+7}_{-8}	$28.3^{+4.7}_{-2.5}$
J1157+3220	0.011074	392^{+2}_{-2}	$19.46^{+0.12}_{-0.11}$	$5.0^{+0.1}_{-0.2}$	$0.56^{+0.03}_{-0.02}$	118^{+1}_{-1}	$33.6^{+4.8}_{-0.7}$
J1200+1343	0.066828	131^{+3}_{-3}	$19.23^{+0.17}_{-0.08}$	$4.5^{+0.2}_{-0.1}$	$-0.04^{+0.04}_{-0.04}$	219^{+1}_{-1}	$86.3^{+4.6}_{-3.1}$
J1253-0312	0.022846	131^{+1}_{-1}	$19.28^{+0.02}_{-0.04}$	$4.2^{+0.1}_{-0.1}$	$-3.19^{+0.70}_{-0.69}$	246^{+1}_{-1}	$30.2^{+0.4}_{-0.4}$
J1323-0132	0.022511	26^{+1}_{-1}	$18.22^{+0.06}_{-0.08}$	$3.2^{+0.0}_{-0.1}$	$-0.95^{+0.04}_{-0.05}$	112^{+1}_{-1}	$87.5^{+1.3}_{-1.2}$
J1359+5726	0.033938	175^{+3}_{-2}	$19.30^{+0.13}_{-0.08}$	$4.6^{+0.1}_{-0.2}$	$-0.82^{+0.23}_{-0.18}$	125^{+2}_{-2}	$55.7^{+5.5}_{-2.9}$
J1416+1223	0.123174	-5^{+4}_{-4}	$19.20^{+0.08}_{-0.08}$	$3.6^{+0.6}_{-0.3}$	$0.38^{+0.10}_{-0.10}$	306^{+7}_{-8}	$41.7^{+2.9}_{-2.6}$
J1418+2102	0.008699	21^{+1}_{-1}	$19.73^{+0.05}_{-0.02}$	$4.1^{+0.1}_{-0.1}$	$-3.38^{+0.58}_{-0.76}$	246^{+1}_{-1}	$67.4^{+2.9}_{-2.9}$
J1428+1653	0.181544	122^{+2}_{-3}	$19.23^{+0.05}_{-0.09}$	$3.0^{+0.2}_{-0.1}$	$0.21^{+0.07}_{-0.08}$	168^{+2}_{-3}	$46.5^{+3.3}_{-3.4}$
J1429+0643	0.173649	21^{+2}_{-2}	$19.95^{+0.09}_{-0.04}$	$3.4^{+0.2}_{-0.1}$	$-1.30^{+0.06}_{-0.05}$	321^{+5}_{-6}	$41.6^{+2.1}_{-2.1}$
J1521+0759	0.094335	141^{+3}_{-4}	$19.40^{+0.08}_{-0.08}$	$5.0^{+0.1}_{-0.1}$	$-1.21^{+0.22}_{-0.23}$	97^{+4}_{-4}	$9.5^{+1.1}_{-0.7}$
J1525+0757	0.075916	133^{+1}_{-2}	$18.58^{+0.09}_{-0.07}$	$4.7^{+0.1}_{-0.2}$	$-1.09^{+0.12}_{-0.11}$	44^{+2}_{-2}	$20.1^{+1.0}_{-1.0}$
J1545+0858	0.037834	92^{+2}_{-3}	$19.43^{+0.06}_{-0.06}$	$4.2^{+0.1}_{-0.2}$	$-1.87^{+0.34}_{-0.40}$	72^{+3}_{-2}	$37.0^{+1.8}_{-1.1}$
J1612+0817	0.149198	187^{+4}_{-2}	$19.79^{+0.08}_{-0.07}$	$5.0^{+0.2}_{-0.2}$	$0.42^{+0.03}_{-0.02}$	84^{+2}_{-2}	$94.9^{+5.1}_{-4.8}$

Note. (1) Object name; (2) redshift estimated by the shell model; (3) outflow velocity of expanding shell; (4) H I column density; (5) temperature; (6) dust extinction; (7) intrinsic line width; (8) equivalent width.

(This table is available in machine-readable form.)

DLA system at $N_{\rm H\,I} \approx 10^{21}$ cm^{-2}. We recognize that the DLA sightlines and the pathways of the scattered Lyα emission select specific channels through a turbulent, multiphase ISM. Nonetheless, their combined distribution may represent a large fraction of all sightlines because we found that these components cover complementary fractions of the UV continuum (see Sections 2 and 3).

We weight the column densities by the covering fraction of each system in the middle panel of Figure 11. This normalization indicates how many sightlines are covered by the low-$N_{\rm H\,I}$ or high-$N_{\rm H\,I}$ paths. After accounting for the covering fraction, the peak of the distribution of low-$N_{\rm H\,I}$ paths shifts to a lower-column density; the lower-column densities have higher weights, i.e., larger covering fraction of low-$N_{\rm H\,I}$ paths. In other words, the galaxies with only Lyα emission line observed have lower-column densities compared to those showing Lyα emission in the bottom of DLA system.

In the bottom panel, we present the combined distribution of column densities in galaxies with only Lyα emission, only DLA system, or Lyα emission in the bottom of DLA system. Similar to the middle panel, the distributions are weighted by the covering fraction. Clearly, the column densities increase with the presence of DLA system, consistent with the middle panel. Overall, however, the distribution remains bimodal, consistent with the argument that the distribution includes a large fraction of all sightlines. At a qualitative level, the bimodal distributions in Figure 11 confirm a structural similarity between the ISM in CLASSY galaxies and the ISM in hydrodynamical simulations focusing on the star—gas interplay (Ma et al. 2020; Kakiichi & Gronke 2021). In detail, however, we recognize several quantitative differences.

4.1.2. Column Density Distribution in Simulations

In the H II region simulations of Kakiichi & Gronke (2021), turbulence driven by ionization fronts creates a bimodal distribution of column densities. In their Figure 6, the higher-column-density peak covers $N_{\rm H\,I}$ values similar to our Figure 11. The simulated column density distribution actually reaches a minimum around 10^{19} cm^{-2}, however, right where where Figure 11 shows a maximum. The lower-column-density peak is offset to 10^{17} cm^{-2} in the simulated distribution. These simulations zoom in on the individual H II region, and it is

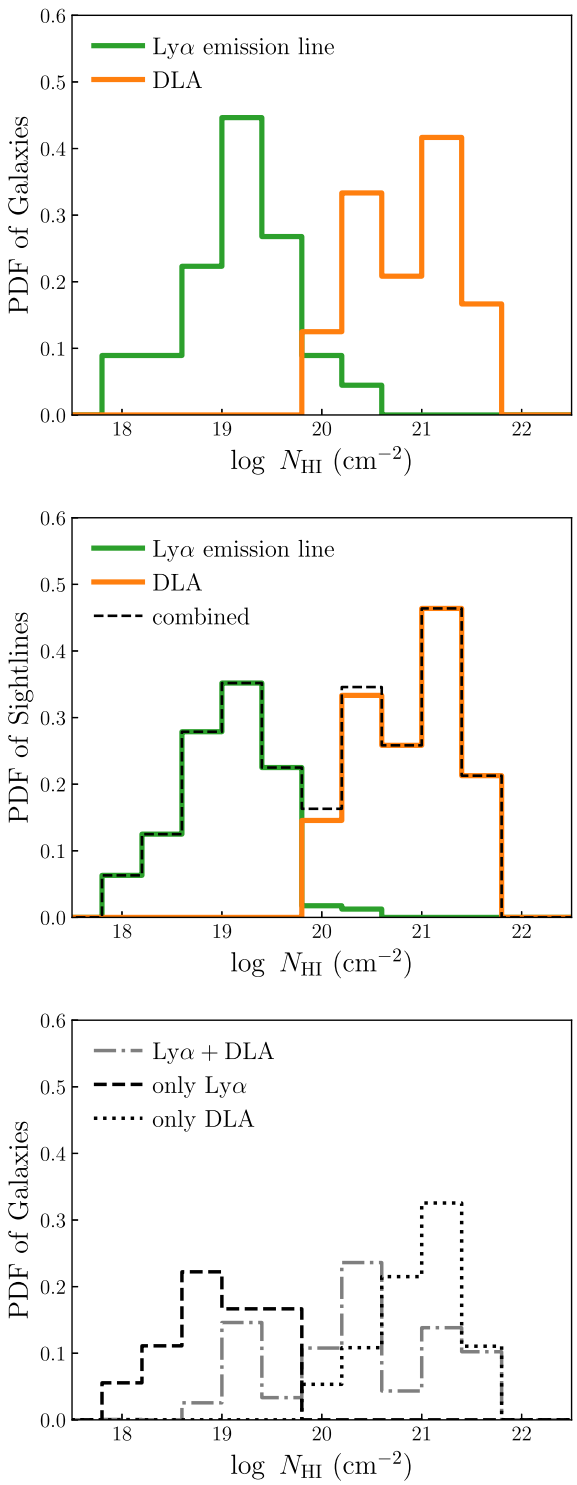

Figure 11. The probability distribution functions of column densities derived by the DLA fitting (orange line) and the Lyα profile fitting (green line). In the top panel, the histograms are normalized by the total numbers of galaxies showing DLA system (31) or Lyα emission line (28 after excluding the J0808 +3948 active galactic nucleus), respectively. In the middle panel, the histogram is weighted by the covering fraction of low-$N_{\rm H\,I}$ and high-$N_{\rm H\,I}$ paths: $(1-f_C)$ and f_C, respectively. The black dashed line represents the combined distribution over the $\sim 10^{18}$–10^{22} cm^{-2} range for CLASSY galaxies. In the bottom panel, we present the distribution of column densities for three types of Lyα profiles. The black dashed line indicates the galaxies with only Lyα emission, the gray dashed–dotted line indicates the galaxies with Lyα emission in the bottom of DLA system, and the dotted line indicates the galaxies with only DLA systems. The resulting distribution remains bimodal regardless of the details of the weighting and subsample.

possible that placing the H II region in a more realistic galactic environment would shift the distribution.

Comparing the histogram in Figure 11 to those from Figure 11 of Ma et al. (2020), we find the high-$N_{\rm H\,I}$ gas spread over a similar range in column density. In those simulations, the fraction of high-$N_{\rm H\,I}$ is sensitive to galaxy mass; for their 10^7–10^8 $M_\odot$ sample, the fraction of sightlines with high-$N_{\rm H\,I}$ to the total H I sightlines is about one-third as large seen in Figure 11. Since their histograms exclude the gas within $0.2R_{\rm vir}$ of the starburst, it is possible that the addition of the starburst region would eliminate, or at least mitigate, the discrepancy. Another difference is the column density of the lower-density peak. This peak is seen at $N \approx 18$–20 cm^2 in CLASSY, whereas Ma et al. (2020) find the low-$N_{\rm H\,I}$ channels spread, primarily, over the $N \approx 16$–18 cm^2 range. This result may indicate that the feedback in Ma et al. (2020) is too efficient and removes too much neutral hydrogen.

Integral-field spectroscopy is clearly needed to address two observational biases. The histograms in Figure 11 combine measurements made on different physical scales because the physical size of the aperture changes with galaxy distance. It is not fully understood how the aperture affects the column density derived by shell-model fitting. In addition, we emphasize that the lowest-column density sightlines may be missing from Figure 11. The shell model returns a column density that represents the total column of clouds plus an intercloud medium (Li & Gronke 2022); it follows that the lowest- (and highest-) column density sightlines may not be represented in Figure 11. The low-$N_{\rm H\,I}$ channels may therefore include lower-column-density pathways, and we aim to understand whether CLASSY galaxies have sightlines optically thin to LyC radiation.

4.2. Pathways for LyC Leakage

In this section, we will investigate the LyC-thin sightlines[24] with $N_{\rm H\,I} < 10^{18}$ cm^{-2} in CLASSY sample by analyzing the positive residual Lyα trough fluxes and small $\Delta v_{\rm Ly\alpha}$.

4.2.1. Peak Separation, Trough Flux, and Red Asymmetry

Peak separation is a good, empirical tracer of LyC escape (Izotov et al. 2020), and the shell model provides a theoretical basis for this relation (Dijkstra et al. 2016; Eide et al. 2018). In galaxies where there are few holes through which LyC can escape (low LyC leakage), the scattered Lyα photons traverse optically thick channels, leading to a broad peak separation. Whereas, in galaxies with high LyC leakage, the density-bounded channels result in a small peak separation. However, the peak separation does not distinguish how the Lyα photons escape (Kakiichi & Gronke 2021), as many small holes in a turbulent medium can produce a narrow peak separation just like a large, wind-blown cavity.

The Lyα asymmetry parameter A_f helps to quantify the multiphase nature of the turbulent H II regions. It is originally introduced by Rhoads et al. (2003) to measure the attenuation imprinted by IGM at high-redshift. Here, we apply it in a different context recently introduced by Kakiichi & Gronke (2021). The two dominant types of Lyα escape (single flight or excursion) tend to produce a symmetric Lyα line. Thus, when the medium is dominated either by ionization- or density-

[24] Column densities lower than 10^{18} cm^2 correspond to LyC escape fractions $\gtrsim$1% (Kakiichi & Gronke 2021).

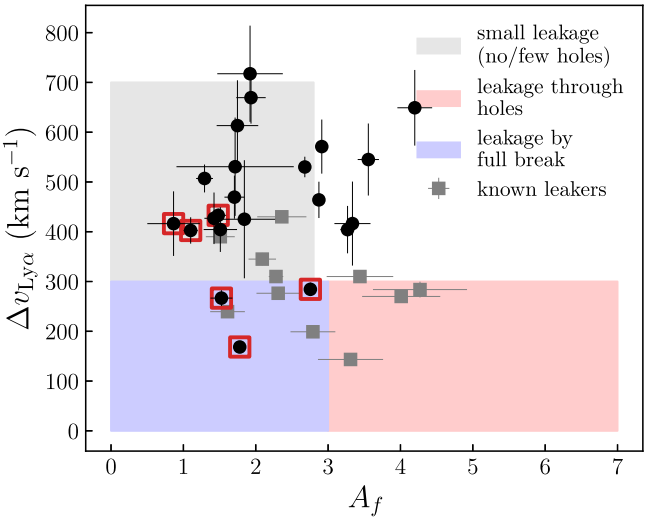

Figure 12. Lyα red peak asymmetry vs. Lyα peak separation. The gray, blue, and pink shaded regions correspond to three different regimes of LyC leakage: small leakage (gray), leakage through low-$N_{\rm H\,I}$ holes (small holes, red), and leakage by the full break (large density-bounded holes, blue), respectively. We overplot the known leakers from Izotov et al. (2016, 2018a, 2018b) as gray squares. The red squares highlight six galaxies (J0942+3547, J0944-0038, J1253-0312, J1323-0132, J1418+2102, J1545+0858), which have net Lyα trough flux, suggesting they might be LyC leakers.

bounded channels as in the blue or gray region in Figure 12, the asymmetry of the emergent line is low. However, when the two channels coexist as in the red region in Figure 12, the asymmetry is high.

In Figure 12, we plot Lyα peak separation against red peak asymmetry. We divide the diagram into three distinct regions: (gray) low LyC leakage, (red) significant leakage through low-$N_{\rm H\,I}$ channels (ionization-bounded, $f_{\rm esc}^{\rm LyC} > 10\%$), and (blue) significant through large holes (density-bounded, $f_{\rm esc}^{\rm LyC} > 10\%$). The boundaries come from Figure 13 of Kakiichi & Gronke (2021), which shows these regions in the $\Delta v_{Ly\alpha}$–$f_{\rm esc}^{\rm LyC}$ and A_f–$f_{\rm esc}^{\rm LyC}$ planes. We find that the strongest LyC leakers in CLASSY are the three galaxies—J0942+3547, J1323-0312, J1545+0858—in the blue region.

The Lyα profiles of these three galaxies also show residual fluxes at Lyα trough: $F_{\rm trough}/F_{\rm cont} = 1.36 \pm 0.07$, 19.62 ± 0.42, 0.17 ± 0.12, respectively. Their net Lyα trough flux supports the conclusion that these galaxies have LyC-thin sightlines (Verhamme et al. 2015; Gazagnes et al. 2020). Based solely on their Lyα profile properties then, these galaxies are likely strong LyC leakers. When we compare their location in Figure 12 to directly confirmed LyC leakers, we find that their peak separation is as small as the smallest values measured among directly confirmed LyC leakers (Izotov et al. 2016, 2018a, 2018b).

Many CLASSY galaxies are located in the gray-shaded region of Figure 12, suggesting they have lower LyC escape fractions than the three galaxies in the blue zone. Three known leakers from Izotov et al. (2016, 2018a, 2018b) also lie in the gray zone of Figure 12, just 100 km s^{-1} above the blue–gray boundary. Based on this comparison to the Lyα properties of the known leakers, we suggest that the CLASSY sample contains more LyC leakers than the (blue) shaded region indicates. The Kakiichi & Gronke (2021) simulations zoom in on individual H II regions, so perhaps, the boundary might shift 100 km s^{-1} in more realistic environments, i.e., those composed of multiple H II regions.

To gain insight into the empirical boundary, we inspect the positions of the other three CLASSY galaxies with net Lyα trough flux. Nonzero trough flux in the emission-line profile requires a low-$N_{\rm H\,I}$ column at the systemic velocity. We find three more galaxies with net trough flux, and each has $\Delta v_{Ly\alpha} < 400$ km s^{-1}. The galaxies are J0944-0038, J1253-0312, and J1418+2102; their trough fluxes are $F_{\rm trough}/F_{\rm cont} = 0.47 \pm 0.29$, 0.22 ± 0.07, 1.46 ± 0.17, respectively.

We acknowledge that Lyα trough fluxes are sensitive to the spectral resolution, which is not precisely known for the Lyα emission. We therefore compared the Lyα trough width to the width of the red peak, which represents an upper limit on the unresolved linewidth. Four galaxies (0942+3547, J1323-0312, J1545+0858, J1418+2102) show broader Lyα trough widths than the Lyα peak widths, so these troughs are clearly resolved. For the other two objects, J0944-0038 and J1253-0312, their Lyα trough widths are similar to Lyα peak widths, so higher-resolution spectroscopy might find that we possibly overestimate their residual trough flux. Consequently, we identified at least four CLASSY galaxies containing density-bounded channels.

We conclude that the empirical boundary between the blue and gray zones lies closer to a peak separation of 400 km s^{-1}, roughly 100 km s^{-1} larger than the blue–gray boundary suggested by the simulations. Based solely on the properties of Lyα line profiles, we conclude that four to six of the CLASSY galaxies (highlighted by red squares in Figure 12) are strong LyC leakers. Their red peaks have a low asymmetry, $A_f < 3$, which indicates they are best described as density-bounded galaxies. In contrast, even though they span the same range of peak separations, half of the directly confirmed leakers have $A_f > 3$, suggesting their leakage is through ionization-bounded channels in a multiphase medium.

4.2.2. *Combining Perspectives from Lyα and O32*

In the previous section, we have shown that the Lyα trough flux, Lyα peak separation, and Lyα red peak asymmetry converge at the same selection of galaxies with density-bounded holes in their neutral ISM. Here, we examine the ionization structure of these galaxies, as measured by optical nebular emission lines, to reveal the underlying relation between LyC leaking channels and ionization. We adopt [O III] λ5007/[O II] λ3727 (O32) ratio, one of the most important ionization diagnostics (Kewley et al. 2019), where a high O32 ratio can indicate a density-bounded galaxy[25] (Jaskot & Oey 2013; Nakajima & Ouchi 2014; Izotov et al. 2016; Flury et al. 2022).

$f_{\rm esc}^{Ly\alpha}$ and O32. Intuitively, we expect a high escape fraction of Lyα photons from density-bounded galaxies. Yet, in the top panel of Figure 13, the O32 ratio shows no correlation with $f_{\rm esc}^{Ly\alpha}$ (Spearman coefficient $\sim$0.04), contradicting the correlation observed among high-redshift galaxies (Trainor et al. 2019) and among local dwarf galaxies (Hayes et al. 2023). We argue here that the lack of correlation in our sample might result from the scattering of Lyα photons outside the COS aperture, an effect that we argued produces DLA systems in many CLASSY spectra (see Section 2.2).

[25] Two of our three best candidates for density-bounded galaxies, J1323-0312 and J1545+0858, have the largest O32 ratios among the CLASSY sample (37.8 and 8.6, respectively). On the other hand, J0942+3547 has a lower O32 ratio of 2.6.

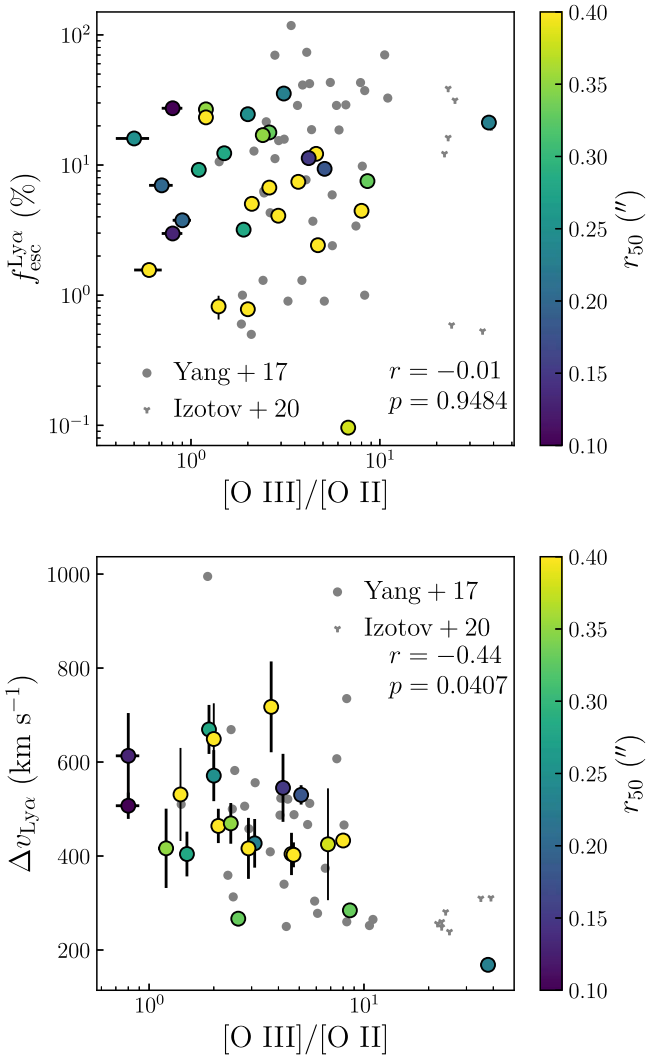

Figure 13. $f_{\rm esc}^{{\rm Ly}\alpha}$ (top) and $\Delta v_{{\rm Ly}\alpha}$ (bottom) vs. O32 ratio. The O32 ratio is defined as [O III] λ5007/[O II] λ3727. We color-code the circles based on their UV half-light radius. The yellow circles have a UV half-light radius larger than 0.″4, which corresponds to the COS unvignetting aperture. We overplot the data in the literature to expand the dynamic range. The gray dots indicate the dwarf galaxies at $z \sim 0.1$–0.4 from Yang et al. (2017). The gray Y-shape markers indicate the local dwarf galaxies at $z \sim 0.02$–0.07 with extreme O32 ratios from Izotov et al. (2020).

The slits used to observe high-redshift galaxies in Trainor et al. (2019) typically subtend 5 to 10 kpc, much larger than the physical scale subtended by the COS aperture for the lowest-redshift targets. Although the *Lyman Alpha Spectral Database* (LASD; Runnholm et al. 2021; Hayes et al. 2023) includes some low-redshift galaxies, the CLASSY sample has a lower median redshift than LASD, so scattering outside the COS aperture plausibly introduces a more serious bias. To test this explanation, we restrict the analysis to the subsample with UV radius <0.″4, the radius of the unvignetted COS aperture, and find a positive correlation; among the yellow points in Figure 13, the Spearman coefficient of 0.22.

However, the galaxy distance might not be the only factor influencing scattering outside the spectroscopic aperture. The Lyα escape fraction of higher-redshift galaxies may also be significantly affected. In the top panel of Figure 13, we overplot measurements for Green Pea galaxies at redshift 0.1–0.4 (Yang et al. 2017). We add LyC leakers from Izotov et al. (2020) with extreme O32 ratios (ranging from 22 to 39). Although the joint sample has a similar redshift range as Hayes et al. (2013), it also shows no correlation between $f_{\rm esc}^{{\rm Ly}\alpha}$ and O32 ratio. A subset of the joint targets with a large O32 ratio has modest $f_{\rm esc}^{{\rm Ly}\alpha}$ of $\sim$1%. Thus, using $f_{\rm esc}^{{\rm Ly}\alpha}$ to probe the density-bounded channels should always be aware of those exceptions, not only the aperture loss.

$\Delta v_{{\rm Ly}\alpha}$ and O32. Consistent with previous studies (Yang et al. 2017; Jaskot et al. 2019; Izotov et al. 2020; Hayes et al. 2023), the Lyα peak separation $\Delta v_{{\rm Ly}\alpha}$ among CLASSY galaxies is anticorrelated with the O32 ratio, as shown in the bottom panel of Figure 13. Excluding the galaxies with large UV radius (>0.″4) does not change the correlation strength, and thus, we conclude that the Lyα peak velocity measurements are only weakly affected by the aperture loss. The Lyα profiles of LyC leakers with extreme O32 ratios of 22–39 from Izotov et al. (2020) show $\Delta v_{{\rm Ly}\alpha} \approx 250$ km s^{-1}, similar to the J1545+0858 and J0942 +3547 in CLASSY sample, consistent with a minimum $\Delta v_{{\rm Ly}\alpha}$ around 250 km s^{-1}. The only data in Figure 13 with lower $\Delta v_{{\rm Ly}\alpha}$ our new data point for J1323-0312.

The joint sample shows that high O32 galaxies always have narrow peak separations, while the low O32 galaxies spread a large range of $\Delta v_{{\rm Ly}\alpha}$. We argue that a high O32 ratio traces a large global covering fraction of LyC-thin sightlines, whereas the narrow Lyα peak separations appear when the covering fraction of LyC-thin sightlines in our direction is high. The variations in the direction of LyC-thin sightlines relative to our viewing angle, therefore, produce the scatter observed in the $\Delta v_{{\rm Ly}\alpha}$ versus O32 ratio diagram.

The correlation between $\Delta v_{{\rm Ly}\alpha}$ and O32, and the non-correlation between $f_{\rm esc}^{{\rm Ly}\alpha}$ and O32 might hint that the different Lyα features probe Lyα photons from different channels. This speculation is in line with the simulations of Kakiichi & Gronke (2021). When the pathways for LyC escape have a low covering fraction, the majority of Lyα photons still need to escape through low-$N_{\rm H\,I} \approx 10^{18}$–$10^{20}$ cm^{-2} channels, the Lyα emission line emerges with a broad width and large peak separation. Meanwhile, a smaller fraction of Lyα photons will pass through the remaining columns, which are optically thin to the LyC ($<10^{18}$ cm^{-2}), and these sightlines contribute Lyα emission with narrow lines and small peak-separation (see Figure 12 in Kakiichi & Gronke 2021). It follows that the transition from ionization-bounded leakers to density-bounded leakers is accompanied by a change in the shape of the Lyα profiles (namely, the relative strength of the narrow and broad lines). As the covering fraction of LyC thin holes increases, more of the emergent Lyα flux is contributed by the component with narrow peaks. When the intensities of two narrow peaks are larger than those of broad peaks, these LyC thin channels can determine $\Delta v_{{\rm Ly}\alpha}$ while the covering fraction of channels with $>10^{18}$ remains significant and continues to produce broad peaks with a wider separation. Thus, in the case of a significant covering fraction of LyC-thin holes, the peak separation is probing the H I column in LyC-thin holes, and we expect O32 to increase as $\Delta v_{{\rm Ly}\alpha}$ decreases. However, in the case of no LyC leakage or a small LyC leakage, the Lyα photons that pass through the columns $>10^{18}$ cm^{-2} dominate the Lyα profile (peaks and wings).

4.3. Outflow Velocity of Neutral ISM

Chevalier & Clegg (1985) described an adiabatic galactic wind that could reach speeds of roughly 1000 km s^{-1}.

Theoretical models that explain the relation of this hot phase to the widely observed cool outflows have been a subject of studies for an extended period of time (Klein et al. 1994; Schneider & Robertson 2018; Fielding & Bryan 2022). Photoionization modeling of the LIS absorption lines in CLASSY spectra indicates the outflowing component traces gas in which hydrogen is mostly ionized (Xu et al. 2022). Yet, the combined neutral and molecular phases transport as much (or more) mass than does the warm-ionized phase in the outflow from M82 (Martini et al. 2018; Yuan et al. 2023).

Since Lyα probes the portion of the outflow where hydrogen is neutral, the outflow detection using Lyα complements studies of the highly ionized outflow. When Lyα photons scatter in outflowing gas, the resonance center will move blueward with respect to the rest-frame Lyα line center. Consequently, the outflow velocity is imprinted on the Lyα profile. Here, we suggest that the $v_{\rm trough}^{\rm Ly\alpha}$ indicates the average outflow velocity v of neutral clouds, where $-v$ corresponds to the largest optical depth (Orlitová et al. 2018; Michel-Dansac et al. 2020; Li & Gronke 2022). In this section, we first compare Lyα trough velocity $v_{\rm trough}^{\rm Ly\alpha}$ against the Doppler shift of LIS lines. Then, we compare the outflow speeds of neutral ISM in low-$N_{\rm H\,I}$ channels, Lyα trough velocity $v_{\rm trough}^{\rm Ly\alpha}$, to tracers of high-$N_{\rm H\,I}$ clouds. Finally, adopting $v_{\rm trough}^{\rm Ly\alpha}$ as a direct measurement of the mean Doppler shift of the neutral gas, we revisit why radiative-transfer modeling is typically driven toward a shell velocity faster than $v_{\rm trough}^{\rm Ly\alpha}$.

4.3.1. Lyα Trough Velocity and LIS Velocity

Resonance UV absorption lines, e.g., Si II and C II, have been extensively used to measure outflow speeds (e.g., Henry et al. 2015; Reddy et al. 2016; Orlitová et al. 2018; Hayes et al. 2023). Here, we focus on Si II λ1260, which is well measured by the CLASSY collaboration.

The Doppler shifts of Si II in the CLASSY sample have been measured using two different methods. Xu et al. (2022) use a double-Gaussian profile to deblend the outflow component from the static ISM component of Si II and find that the outflow component is mostly ionized. On the other hand, K. Parker et al. (2023, in preparation) fit a single-Voigt profile to determine the average velocity of all LIS absorbers. As the LIS lines can also arise from the neutral ISM, the Parker measurements should include the contribution of neutral ISM. Conceptually, if the LIS absorber is dominated by the static ISM, the Parker measurement, which is close to 0 km s^{-1}, should be distinct from the Xu measurement. But if the LIS absorber is dominated by the outflow component, the Parker measurement should be similar to the Xu measurement.

Figure 14 presents the comparisons of $v_{\rm trough}^{\rm Ly\alpha}$ to both LIS outflow measurements derived by the two methods.[26] Directly comparing the two LIS outflow measurements in the top and bottom panels, we notice the positions of two objects (J1416+1223, J0938+5428) shift significantly. K. Parker et al. (2023, in preparation) derive a velocity close to 0 km s^{-1}, but the outflow velocities derived in Xu et al. (2022) can reach several hundred kilometers per second, suggesting the LIS absorbers of these two galaxies are mainly static. The galaxies that shift between the two panels have substantial absorption at $v = 0$, which we attribute to the static ISM.

[26] J0808+3948 is excluded because its polycyclic aromatic hydrocarbon feature suggests it might be an active galactic nucleus (Xie et al. 2014).

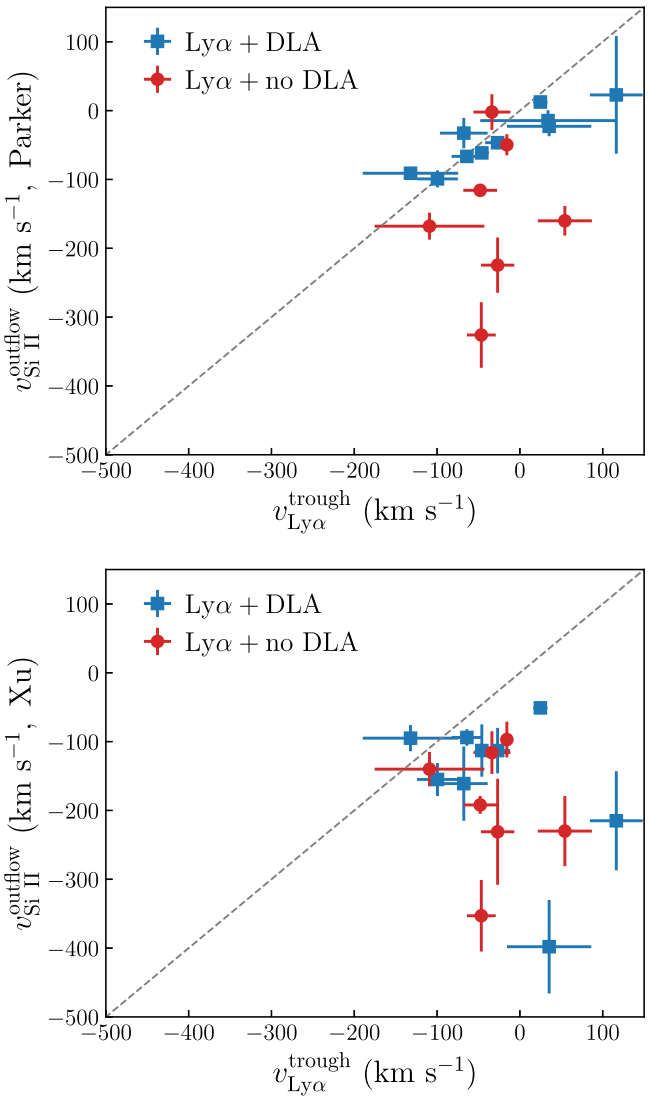

Figure 14. $v_{\rm Si\,II}^{\rm outflow}$ vs. $v_{\rm trough}^{\rm Ly\alpha}$. The top panel adopts the $v_{\rm Si\,II}^{\rm outflow}$ measured by the single-Voigt fitting (K. Parker et al. 2023, in preparation), and the bottom panel adopts the $v_{\rm Si\,II}^{\rm outflow}$ measured by a double-Gaussian fitting (Xu et al. 2022). The dashed lines indicate the 1:1 relationship. The Si II absorbers are multiphase, including neutral hydrogen in addition to the mostly ionized phase. By comparing $v_{\rm trough}^{\rm Ly\alpha}$ and $v_{\rm Si\,II}^{\rm outflow}$, we are able to distinguish ionization status of the ISM.

Second, we see that the Si II velocity measured by K. Parker et al. (2023, in preparation) shows a better agreement with $v_{\rm trough}^{\rm Ly\alpha}$, particularly the galaxies with both Lyα and DLAs (blue squares) in the top panel of Figure 14. This suggests that, in those galaxies, the Si II absorbers (in both outflow and static) contain a significant fraction of neutral hydrogen, although Xu et al. (2022) suggest that the Si II in the outflow traces mostly ionized gas.

However, looking at the galaxies with no DLAs (red circles in Figure 14), their Si II velocities disagree with $v_{\rm trough}^{\rm Ly\alpha}$ in both two panels. The three most deviant circles (J0021+0052, J0926+4427, J1429+0643) show that their $v_{\rm trough}^{\rm Ly\alpha}$ are close to 0 km s^{-1}, but the Si II velocities are $\leqslant -200$ km s^{-1}. We find that their Si II line profiles are dominated by the outflow component: they have very little absorption at the systemic velocity, so the velocity is not sensitive to the measurement method. This suggests that the Si II absorption comes mostly

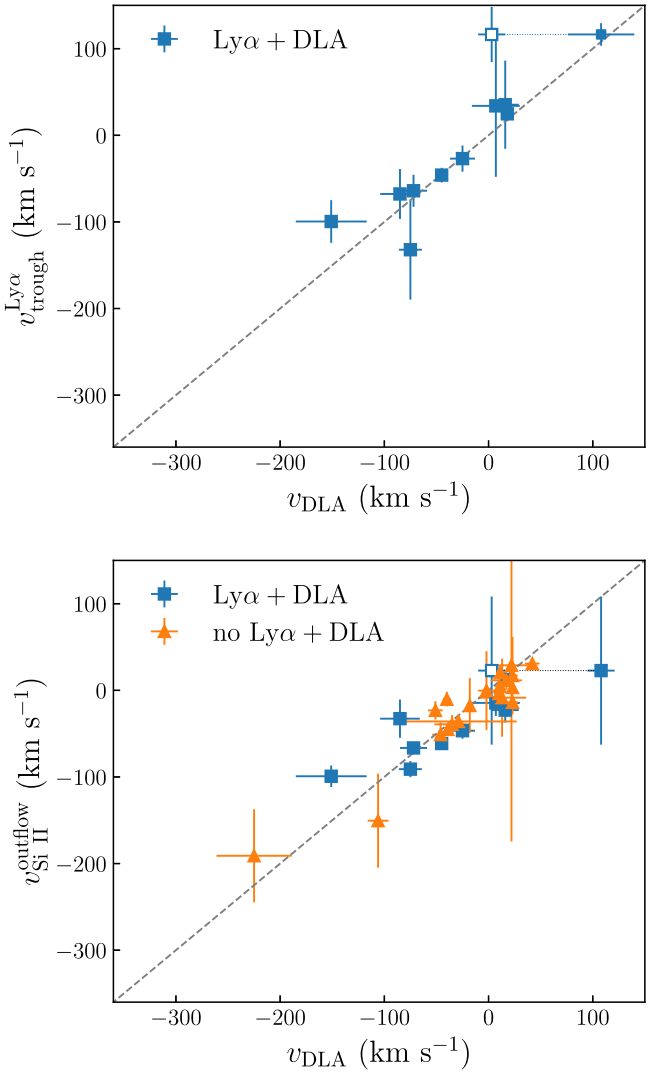

Figure 15. v_{DLA} vs. $v^{\mathrm{Ly}\alpha}_{\mathrm{trough}}$ (top) and $v^{\mathrm{outflow}}_{\mathrm{Si\ II}}$ (bottom). Here, we adopt the $v^{\mathrm{outflow}}_{\mathrm{Si\ II}}$ measured by K. Parker et al. (2023, in preparation). The gray dashed lines indicate the 1:1 relationship. In the bottom panel, we separate the sample based on whether their spectra have Lyα emission lines. We notice the O I absorption line of one galaxy (J0938+5428, open square) is contaminated by the refilling O I emission line. Thus, we adopt the velocity of C II absorption line, and we use a black dashed line to connect them. The good agreement suggests that the gas in low-$N_{\mathrm{H\ I}}$ has same velocity as the gas in high-$N_{\mathrm{H\ I}}$ channels.

from the ionized gas in these galaxies, similar to Xu et al. (2022).

4.3.2. Lyα Trough Velocity and DLA Velocity

In the top panel of Figure 15, we compare the Lyα trough velocity $v^{\mathrm{Ly}\alpha}_{\mathrm{trough}}$ and the velocity of high-$N_{\mathrm{H\ I}}$ clouds (i.e., DLA system velocity probed by O I absorption line). It is intriguing to see such a good agreement between these two independent measurements, suggesting that the low-$N_{\mathrm{H\ I}}$ channels have the same velocity as the high-$N_{\mathrm{H\ I}}$ channels.

In the bottom panel of Figure 15, we further find that DLA velocity agrees with Si II velocity. Here, we include the galaxies, which do not have Lyα emission lines, as the circles. They are consistent with those galaxies that have both Lyα emission lines and DLA systems. This hints that, for the galaxies with DLA systems, the intrinsic reason for the correlation between Si II velocity and $v^{\mathrm{Ly}\alpha}_{\mathrm{trough}}$ is that the Si II mainly traces the high-$N_{\mathrm{H\ I}}$ clouds, and the high-$N_{\mathrm{H\ I}}$ clouds have similar velocity as the low-$N_{\mathrm{H\ I}}$ clouds.

4.3.3. Revisiting Outflow Velocity Discrepancy

In this section, we discuss the outflow velocity discrepancy using the same profile fittings as Section 3.3 and propose a new explanation of the discrepancies. Here, we adopt the $v^{\mathrm{Ly}\alpha}_{\mathrm{trough}}$ as the intrinsic outflow velocity since it traces the neutral ISM, which scatters the Lyα photons.

First, we directly compare the $v^{\mathrm{Ly}\alpha}_{\mathrm{trough}}$ measured based on the spectroscopic redshift and the outflow velocities v_{tlac} estimated by the shell model. In the top panel of Figure 16, we present the comparison for both the second profile fitting (redshift-unconstrained) and the third profile fitting (redshift-constrained). Although a clear correlation between $v^{\mathrm{Ly}\alpha}_{\mathrm{trough}}$ and v_{tlac} can be seen, v_{tlac} is larger by 0–200 and 0–140 km s^{-1} than the $v^{\mathrm{Ly}\alpha}_{\mathrm{trough}}$ for the second and third fittings, respectively.

We speculate that the reason for this discrepancy is a *redshift error* required by the model fitting. To test this idea, we shift our $v^{\mathrm{Ly}\alpha}_{\mathrm{trough}}$ measurements to the fictitious reference frame chosen by the fitted tlac redshift.

The bottom panel of Figure 16 shows the $v^{\mathrm{Ly}\alpha}_{\mathrm{trough}}$ measurements in the tlac reference frames defined by the second and third fittings. We have shifted the measurements by

$$v^{\mathrm{Ly}\alpha}_{\mathrm{trough},z_{\mathrm{tlac}}} = v^{\mathrm{Ly}\alpha}_{\mathrm{trough}} - (z_{\mathrm{tlac}} - z_{\mathrm{spec}}) \times c, \quad (5)$$

where c is the speed of light. The new correlations are significantly improved and close to the 1:1 relationship. In particular, for the redshift-unconstrained fitting (second attempt), $v^{\mathrm{Ly}\alpha}_{\mathrm{trough}}$ and v_{tlac} agree well with each other. These results confirm that we should compare $v^{\mathrm{Ly}\alpha}_{\mathrm{trough}}$ and v_{tlac} in a common redshift frame. This also confirms that the outflow velocity and the redshift are coupled in the shell model:

$$\frac{\lambda^{\mathrm{Ly}\alpha}_{\mathrm{trough}}}{(1+z) \times \lambda_{\mathrm{Ly}\alpha}} - 1 = -\frac{v^{\mathrm{outflow}}}{c}, \quad (6)$$

where $\lambda^{\mathrm{Ly}\alpha}_{\mathrm{trough}}$ is the wavelength of Lyα trough, and $\lambda_{\mathrm{Ly}\alpha}$ is the rest-frame wavelength of Lyα. Once the redshift of the shell model is fixed, the model outflow velocity is also determined by the Doppler offset of the observed Lyα trough with respect to the model redshift. Thus, the redshift and outflow velocity discrepancies are the *two sides of the same coin*.

The preferred larger outflow velocity by tlac may hint that the observed B/R ratio is lower than the intrinsic B/R ratio. Moreover, as we discussed in Section 2.2, the observed B/R ratio can be biased by the aperture loss. Thus, this inspires us to connect the discrepancies to the aperture loss.

We, therefore, propose an explanation for the discrepancies. Since the aperture loss modifies the B/R ratio to a lower value and the B/R ratio is tightly anticorrelated with outflow velocity, to achieve the smaller observed B/R ratio, the shell model will suggest a larger outflow velocity. Meanwhile, a higher systematic redshift is required to match the Lyα trough velocity to the outflow velocity (Equation (6)). Thus, the best-fit redshift and outflow velocity from the shell model are larger than that observed from the spectra. The aperture loss has a nonnegligible impact on the Lyα profile and should always be considered when interpreting Lyα profile.

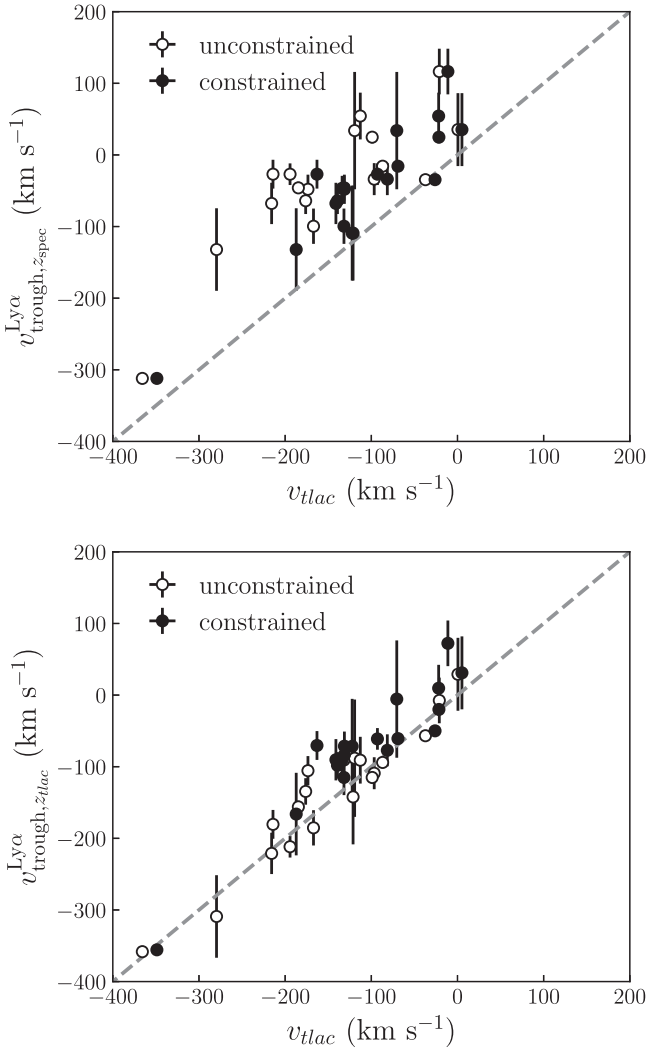

Figure 16. The Lyα trough velocity measured from spectrum vs. the outflow velocity estimated by the shell model. Top panel: the $v^{\mathrm{Ly}\alpha}_{\mathrm{trough}}$ is measured based on the spectroscopic redshift. Bottom panel: the $v^{\mathrm{Ly}\alpha}_{\mathrm{trough}}$ is measured based on the redshift from tlac profile fitting. We plot the measurements from both the z-unconstrained fitting (open circle, Section 3.2.2) and the z-constrained fitting (solid circle, Section 3.3). The dashed line indicates the 1:1 relationship.

4.4. A Schema of the Neutral ISM

In this section, we summarize our interpretation of ISM structure from the previous sections. We have demonstrated that the ISM in CLASSY galaxies is inhomogeneous, consisting of high-$N_{\mathrm{H\,I}}$, low-$N_{\mathrm{H\,I}}$, and even LyC-thin regions, based on the clear separation between the DLA and Lyα emission (see Section 3.2), the nonzero residual flux at Lyα trough, and small peak separation (see Section 4.1). In the left panel of Figure 17, we plot a schema of the neutral ISM for illustration. For simplicity, we adopt a continuous shell model. The low-$N_{\mathrm{H\,I}}$ and high-$N_{\mathrm{H\,I}}$ paths are shown as light blue and dark blue, respectively. We also use two gray shades to indicate the Lyα halos missed due to the aperture effect. In the right panel, we zoom in to show the Lyα radiative transfer in a small slab. The green lines indicate the Lyα photons, and the gray lines indicate the continuum photons.

Although the Lyα radiative process is highly nonlinear and nonadditive, the radiative transfer fitting results suggest that we can take the Lyα emission and DLA system apart. The DLA system can be well fitted by a partial-covering Voigt profile with a high-$N_{\mathrm{H\,I}}$, and the Lyα emission normalized by the uncovered continuum can be well fitted by the shell model with a low-$N_{\mathrm{H\,I}}$. This clear separation between Lyα emission and DLA system indicates that the Lyα exchange between low-$N_{\mathrm{H\,I}}$ path and high-$N_{\mathrm{H\,I}}$ path should be negligible, as we discussed in Section 3.2. Only very few Lyα photons that are injected into one region can travel to another region, and thus, the Lyα radiative processes in two different regions are independent. This is feasible because of two reasons: (1) the possibility of a Lyα photon traveling from low-$N_{\mathrm{H\,I}}$ path to high-$N_{\mathrm{H\,I}}$ path is very small, as most of which are just "reflected" by the surface between two channels (Hansen & Oh 2006); (2) the Lyα photons including the underlying continuum photons that are injected into high-$N_{\mathrm{H\,I}}$ paths are mostly scattered to much larger impact parameters (i.e., the extended Lyα halo, Steidel et al. 2011; Zheng et al. 2011); thus, most of which are missed due to the aperture effect and leave a DLA system. Thus, only the Lyα photons that escape through low-$N_{\mathrm{H\,I}}$ regions can be observed, and the emergent Lyα profile is a combination of Lyα spectra from two regions, as illustrated by the green and gray lines in Figure 17, and has a profile of Lyα emission in the bottom of DLA system.

In the left panel of Figure 17, we plot several low-$N_{\mathrm{H\,I}}$ channels in different directions. Although all of those low-$N_{\mathrm{H\,I}}$ channels can allow the escape of Lyα photons, only the channels exposed to the COS aperture (i.e., horizontal one in Figure 17) can contribute to the observed Lyα emission line. Because, for the Lyα photons that are initially injected into low-$N_{\mathrm{H\,I}}$ channels in other directions, they still need to penetrate the high-$N_{\mathrm{H\,I}}$ paths before reaching us.

We have proposed a scenario that the aperture loss is responsible for those unexpected profiles of Lyα emission in the bottom of DLA system in the CLASSY sample. In this work, we also find that the DLA absorber (neutral gas in high-$N_{\mathrm{H\,I}}$ paths) has a similar systematic velocity as the neutral gas in the low-$N_{\mathrm{H\,I}}$ paths. However, the ionized gas, traced by the outflowing component of Si II absorption line, has a generally larger velocity compared with that of the neutral gas in the low-$N_{\mathrm{H\,I}}$ paths.

Using three LyC leakage diagnostics, we find that at least three galaxies in the CLASSY sample are LyC leaker candidates. Thus, in the right panel of Figure 17, we use yellow to indicate the possible LyC-thin channels in the ISM, through which the Lyα photons can easily escape without much resonant scattering. By comparing the $\Delta v_{\mathrm{Ly}\alpha}$ with O32 ratio, we conclude that the O32 ratio is tracing the covering fraction of LyC-thin channels, consistent with those known LyC leakers (Flury et al. 2022). The covering fraction increases as the O32 ratio increases, and thus, the probability of observing small $\Delta v_{\mathrm{Ly}\alpha}$ increases.

5. Summary and Conclusions

In this paper, we extracted high-resolution Lyα line profiles from CLASSY spectra of 45 EoR analogs. These HST COS/G130M spectra show a wide variety of Lyα profiles, including damped absorption, Lyα emission in DLA profiles, P Cygni profiles, and pure Lyα emission. We attribute the damped absorption to Lyα photons being scattered out of the spectroscopic aperture, and we argue that the especially large diversity among CLASSY Lyα profiles can be largely attributed to large

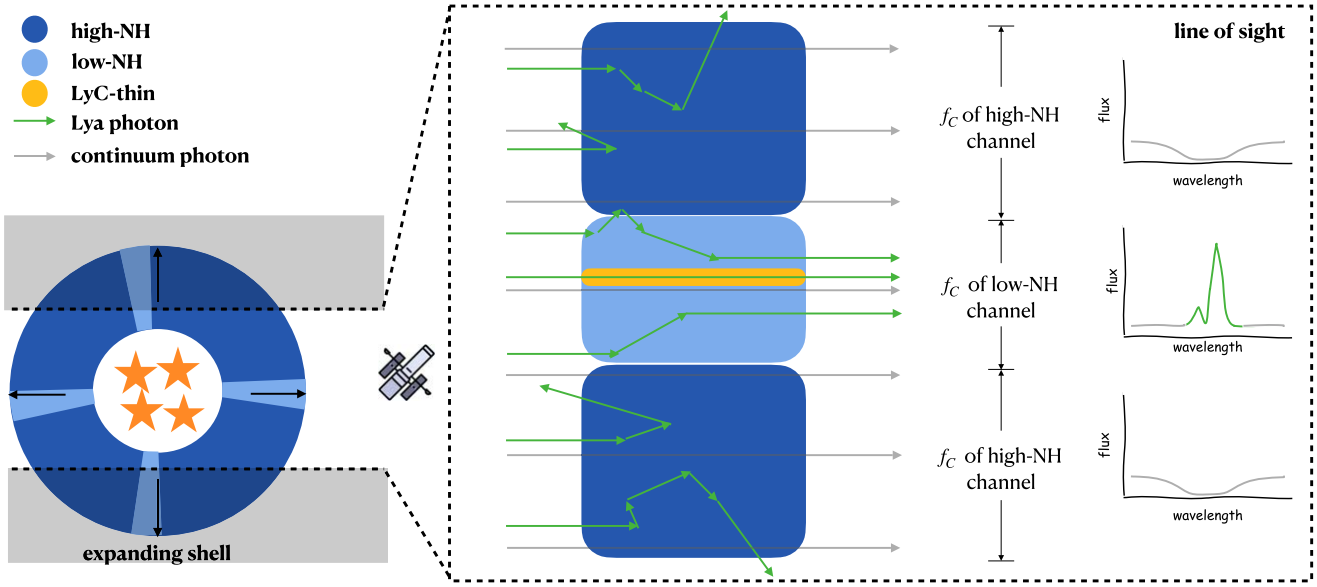

Figure 17. The left panel shows the side view of HST/COS observation. We adopt a continuous shell geometry, which contains different column-density regions as dark blue and light blue. This is somewhat an oversimplification as the ISM can be clumpy, but should be the simplest way to illustrate the ISM in galaxies. We note the scale length of different regions in this figure does not indicate their physical scale length. We use the gray shaded regions to indicate the parts that are missed by the HST/COS aperture. The right panel shows the zoom-in structure of a small slab of the outflowing shell. The yellow, light blue, and dark blue indicate the LyC-thin, low-$N_{\rm H\,I}$, and high-$N_{\rm H\,I}$ paths, respectively. The gray and green lines show the radiative transfer processes of the continuum and Lyα photons. We mark the covering fraction of different column density channels. The rightmost spectra represent the emergent Lyα profiles along different regions. The low-$N_{\rm H\,I}$ channels lead to the Lyα emission line, but the high-$N_{\rm H\,I}$ channels lead to the DLA system. The observed Lyα spectrum is a combination of those Lyα profiles, and thus, the residual flux in the bottom of the DLA profile equals the covering fraction of low-$N_{\rm H\,I}$ channels.

range of physical scales subtended by the COS aperture, a little over 100 pc up to nearly 8 kpc.

We separated the DLA and Lyα emission components of the profiles. Specifically, we adopted the precisely measured Doppler shifts of the O I absorption components as priors for the Doppler shift of each broad DLA profile, and we fitted the damped Lyα absorption with modified Voigt profiles. After subtracting the stellar continuum and the DLA profile, we modeled the Lyα emission profile and the appropriate underlying continuum using the shell model. For the first time, we measure the properties in the neutral shell traversed by the emergent Lyα emission, and the conditions in the high-column density clouds, in the same sample of galaxies. For double-peaked Lyα emission-line profiles, we defined the Doppler shift of the minimum between the two emission lines as the *trough velocity*, which we compared to the Doppler shifts of LIS absorption lines and the DLA. Our results are summarized below:

1. The Lyα emission in the bottom of the DLA profile reveals the inhomogeneity of the ISM and the outflows. The DLA profile and Lyα emission line can be surprisingly well fitted by simply splitting a geometric covering factor between the high-column density sightlines and the lower-$N_{\rm H\,I}$ channels through which Lyα photons escape. This suggests little Lyα exchange between high- and low-$N_{\rm H\,I}$ paths. Combining the sightlines probed by Lyα emission lines with those producing damped absorption, the net distribution of column densities is bimodal and therefore qualitatively similar to the distributions predicted by numerical simulations of H I regions (Ma et al. 2020; Kakiichi & Gronke 2021). It is important to note, however, that this observed distribution is offset to higher $N_{\rm H\,I}$ compared with the simulations. This discrepancy could arise from gas on larger spatial scales than the simulations include, or from structural differences in the star-forming complexes; but, whatever its origin, an understanding of the offset will better inform our understanding of the channels through which not only Lyα but also LyC photons escape from galaxies.
2. We find that the Doppler shift of the Lyα trough velocity matches that of the Si II velocity in most galaxies with DLAs, suggesting that the Si II absorbers in those galaxies are mainly in neutral phase. However, for galaxies without DLA systems, the Lyα trough velocity is always smaller than the Si II velocity, suggesting Si II tracing a more ionized phase of the outflow, consistent with Xu et al. (2022). Thus, the Si II absorbers are multiphase, including neutral hydrogen in addition to the mostly ionized phase. Combining the Lyα and Si II, we are able to identify the ionization of Si II absorbers. Our comparison also suggests that the Lyα trough velocity directly measures the average velocity of neutral gas in the static ISM and outflows.
3. In spectra with a DLA, the Lyα trough velocity agrees well with the DLA velocity (O I velocity), suggesting that the high-$N_{\rm H\,I}$ clouds have similar kinematics as low-$N_{\rm H\,I}$ clouds. Further, the Si II also agrees well with the DLA velocity, even for galaxies without Lyα emission. Thus, we conclude that Si II mainly traces the neutral gas in high-$N_{\rm H\,I}$ columns if the galaxies show DLAs.
4. Motivated by the numerical simulations of Kakiichi & Gronke (2021), we combine the measurements of Lyα peak separation and Lyα red peak asymmetry in a diagnostic diagram that differentiates the type of channels for LyC leakage. Comparing the diagram with the known LyC leakers, we suggest that the boundary for distinguishing substantial leakage from small leakage is a peak

separation less than ∼400 km s^{-1}. In the case of leakage, or equivalently small peak separation, then the red peak asymmetry parameter distinguishes holes, where $A_f > 3$, from the more symmetric profiles generated by full breaks. Six CLASSY galaxies are identified as the density-bounded LyC leakers by this technique, agreeing with the selection of net Lyα trough flux. The inferred properties of the LyC-thin sightlines depend on galaxy orientation, whereas the [O III]/[O II] ratio offers a sightline-independent perspective. We confirm the presence of an inverse relation between Lyα peak separation and the [O III]/[O II] ratio, as has been noted previously (Jaskot et al. 2019; Flury et al. 2022).

5. Similar to Orlitová et al. (2018), we find that the fitted redshift is always larger than the spectroscopic redshift, and the fitted outflow velocity is larger by 10–200 km s^{-1} than the Lyα trough velocity. The connection between the Lyα trough velocity and the outflow velocity offers new insight into the origin of those discrepancies, which we suggest are not adequately explained by parameter degeneracies (Li & Gronke 2022). We argue instead that aperture vignetting is the primary source of the discrepancies. The COS aperture vignettes the blueshifted peak more than the redshifted peak, resulting in a lower blue-to-red peak ratio. To match the lower blue-to-red peak ratio, the radiative transfer model requires a higher outflow velocity and, thus, a larger redshift to match the outflow velocity to Lyα trough velocity.

Our results underline the sensitivity of Lyα profiles to aperture vignetting. The COS aperture not only excludes a large fraction of Lyα photons; it modifies the Lyα profile. Like many CLASSY targets, the composite Lyα spectra of star-forming galaxies at $z \sim 1.8$–3.5 show DLA systems as well (Reddy et al. 2016, 2022). An important difference, however, is that the typical slit width used in ground-based spectroscopy, 1.″2, corresponds to ∼10 kpc. The COS aperture subtends a comparable physical scale only for the most distant Lyman break analogs in CLASSY, and their COS spectra do not show DLAs. Nonetheless, our analysis suggests the DLAs appear in the $z \sim 2$ spectra because the Lyα escape on spatial scales is larger than the slit width. An important implication of this paper is that aperture vignetting could strongly affect recent JWST observation of EoR galaxies using the near infrared spectrograph (NIRSPec) slit mode (Heintz et al. 2023), of which the slit width is just 0.″2, corresponding to only ∼1 kpc.

In this paper, we leveraged these aperture effects, recognizing an opportunity to characterize the properties of the low-$N_{\rm H\,I}$ channels and high-$N_{\rm H\,I}$ clouds in the same set of galaxy sightlines. To fully understand the connection between the observed Lyα profile and LyC leakage, the radiative transfer simulations will need to predict the spatial variations in the profile shape. The extracted Lyα profiles used in this work, including the DLA profiles and the best-fit shell model spectra, can be downloaded from the CLASSY High Level Science Products database, which is developed and maintained at STScI, Baltimore, USA.[27]

Acknowledgments

We thank the anonymous referee for the valuable comments. The CLASSY team is grateful for the support that was provided by NASA through grant HST-GO-15840, from the Space Telescope Science Institute, which is operated by the Associations of Universities for Research in Astronomy, Incorporated, under NASA contract NAS5-26555. C.L.M. thanks the NSF for support through AST-1817125. B.L.J. thanks support from the European Space Agency (ESA). The CLASSY collaboration extends special gratitude to the Lorentz Center for useful discussions during the "Characterizing Galaxies with Spectroscopy with a view for JWST" 2017 workshop that led to the formation of the CLASSY collaboration and survey.

Facility: HST (COS).

Software: astropy (The Astropy Collaboration 2013, 2018), CalCOS (STScI), Python.

Appendix
Best-fit Lyα Spectra

Figures 18 and 19 present the best-fit Lyα spectra obtained using approaches described in Sections 3.2.1 and 3.2.2, respectively.

[27] The data is available at the CLASSY HLSP page at DOI:10.17909/m3fq-jj25 and https://archive.stsci.edu/hlsp/classy.

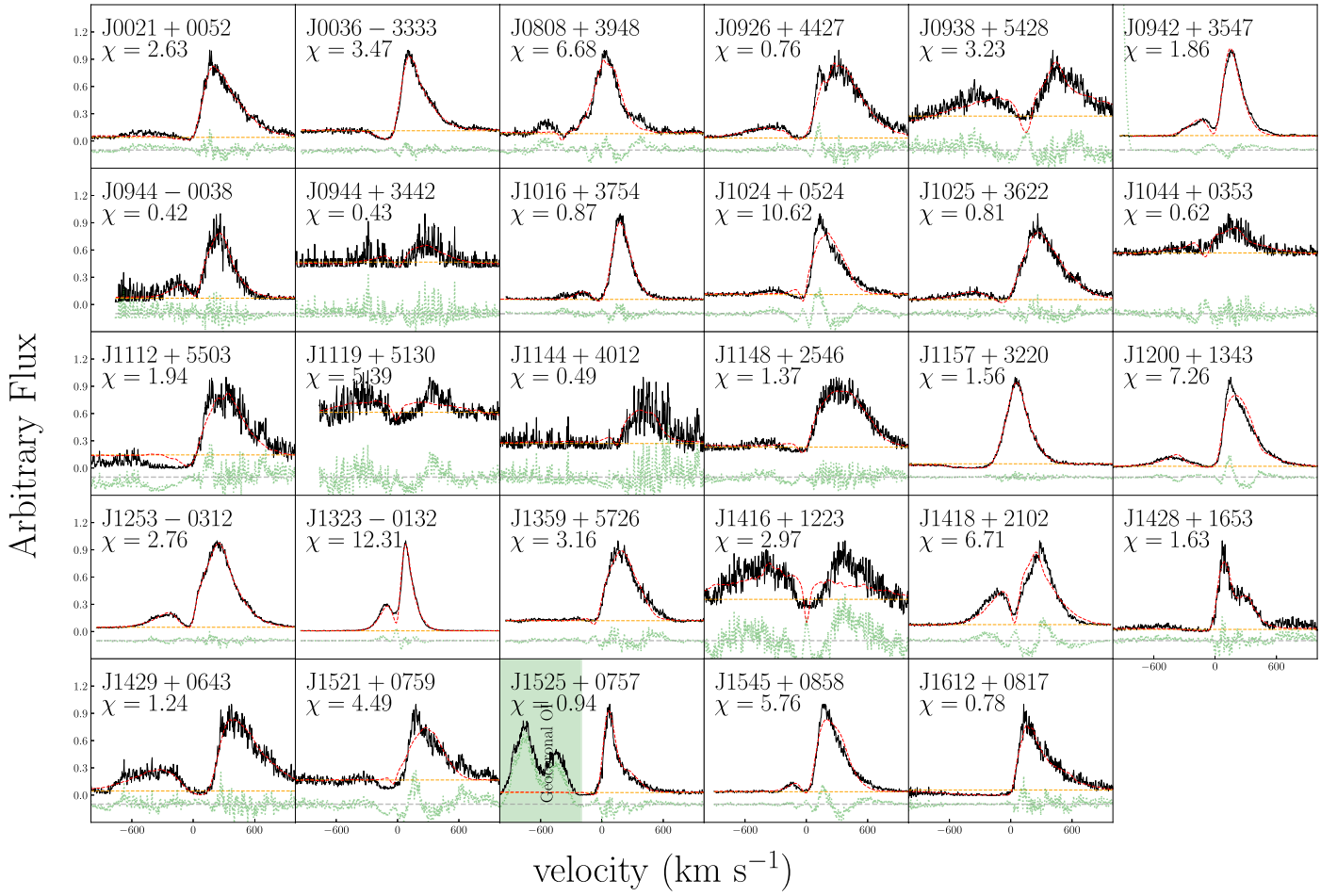

Figure 18. Best-fit Lyα spectra (red) for 29 CLASSY galaxies using the total stellar continuum and a Gaussian redshift prior with $\sigma = 120$ km s^{-1} (first attempt). The spectra are normalized by the peak flux, and the orange dashed lines indicate the continuum level for each object. Clearly, the Lyα spectra of J0938+5428, J0944 +3442, J1044+0353, J1119+5130, J1144+4012, J1416+1223, and J1521+0759 have failed to be reproduced. We use the green lines to show the residual and manually shift it by −0.1 for better illustration. The gray dashed lines indicate the zero level of the residual.

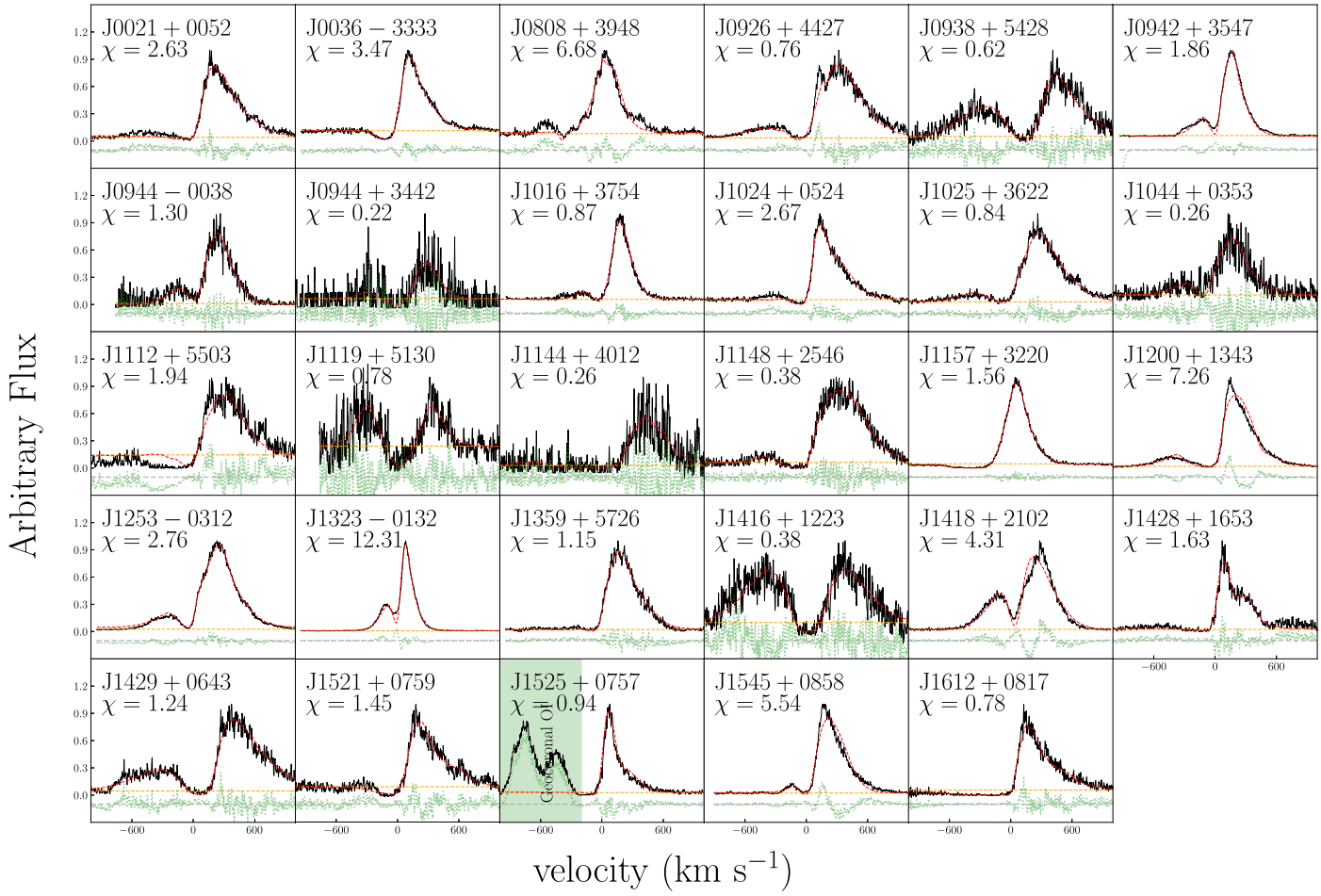

Figure 19. Best-fit Lyα spectra (red) for 29 CLASSY galaxies using the residual stellar continuum and a Gaussian redshift prior with $\sigma = 120$ km s^{-1} (second attempt). The spectra are normalized by the peak flux, and the orange dashed lines indicate the continuum level for each object. Every input Lyα profile is successfully reproduced by tlac model. We use the green lines to show the residual and manually shift it by −0.1 for better illustration. The gray dashed lines indicate the zero level of the residual.

ORCID iDs

Weida Hu https://orcid.org/0000-0003-3424-3230
Crystal L. Martin https://orcid.org/0000-0001-9189-7818
Max Gronke https://orcid.org/0000-0003-2491-060X
Simon Gazagnes https://orcid.org/0000-0002-5659-4974
Matthew Hayes https://orcid.org/0000-0001-8587-218X
John Chisholm https://orcid.org/0000-0002-0302-2577
Timothy Heckman https://orcid.org/0000-0001-6670-6370
Matilde Mingozzi https://orcid.org/0000-0003-2589-762X
Namrata Roy https://orcid.org/0000-0002-4430-8846
Peter Senchyna https://orcid.org/0000-0002-9132-6561
Xinfeng Xu https://orcid.org/0000-0002-9217-7051
Danielle A. Berg https://orcid.org/0000-0002-4153-053X
Bethan L. James https://orcid.org/0000-0003-4372-2006
Daniel P. Stark https://orcid.org/0000-0001-6106-5172
Karla Z. Arellano-Córdova https://orcid.org/0000-0002-2644-3518
Alaina Henry https://orcid.org/0000-0002-6586-4446
Anne E. Jaskot https://orcid.org/0000-0002-6790-5125
Nimisha Kumari https://orcid.org/0000-0002-5320-2568
Kaelee S. Parker https://orcid.org/0000-0002-8809-4608
Claudia Scarlata https://orcid.org/0000-0002-9136-8876
Aida Wofford https://orcid.org/0000-0001-8289-3428
Ricardo O. Amorín https://orcid.org/0000-0001-5758-1000
Jarle Brinchmann https://orcid.org/0000-0003-4359-8797
Cody Carr https://orcid.org/0000-0003-4166-2855
Alessandra Aloisi https://orcid.org/0000-0003-4137-882X

References

Alexandroff, R. M., Heckman, T. M., Borthakur, S., Overzier, R., & Leitherer, C. 2015, ApJ, 810, 104
Astropy Collaboration, Price-Whelan, A. M., Sipőcz, B. M., et al. 2018, AJ, 156, 123
Astropy Collaboration, Robitaille, T. P., Tollerud, E. J., et al. 2013, A&A, 558, A33
Berg, D. A., James, B. L., King, T., et al. 2022, ApJS, 261, 31
Brocklehurst, M. 1971, MNRAS, 153, 471
Bruzual, G., & Charlot, S. 2003, MNRAS, 344, 1000
Bunker, A. J., Saxena, A., Cameron, A. J., et al. 2023, A&A, 677, A88
Cardelli, J. A., Clayton, G. C., & Mathis, J. S. 1989, ApJ, 345, 245
Cash, W. 1979, ApJ, 228, 939
Chevalier, R. A., & Clegg, A. W. 1985, Natur, 317, 44
Chisholm, J., Gazagnes, S., Schaerer, D., et al. 2018, A&A, 616, A30
Chisholm, J., Rigby, J. R., Bayliss, M., et al. 2019, ApJ, 882, 182
Chisholm, J., Tremonti, C. A., Leitherer, C., et al. 2015, ApJ, 811, 149
Dijkstra, M. 2014, PASA, 31, e040
Dijkstra, M., Gronke, M., & Venkatesan, A. 2016, ApJ, 828, 71
Dijkstra, M., Haiman, Z., & Spaans, M. 2006, ApJ, 649, 14
Draine, B. T. 2011, Physics of the Interstellar and Intergalactic Medium (Princeton, NJ: Princeton Univ. Press)
Eide, M. B., Gronke, M., Dijkstra, M., & Hayes, M. 2018, ApJ, 856, 156
Erb, D. K., Li, Z., Steidel, C. C., et al. 2023, ApJ, 953, 118
Erb, D. K., Steidel, C. C., & Chen, Y. 2018, ApJL, 862, L10
Fielding, D. B., & Bryan, G. L. 2022, ApJ, 924, 82

Finkelstein, S. L., D'Aloisio, A., Paardekooper, J.-P., et al. 2019, ApJ, 879, 36
Flury, S. R., Jaskot, A. E., Ferguson, H. C., et al. 2022, ApJ, 930, 126
Gazagnes, S., Chisholm, J., Schaerer, D., Verhamme, A., & Izotov, Y. 2020, A&A, 639, A85
Gordon, K. D., Clayton, G. C., Misselt, K. A., Landolt, A. U., & Wolff, M. J. 2003, ApJ, 594, 279
Gronke, M., Bull, P., & Dijkstra, M. 2015, ApJ, 812, 123
Gronke, M., & Dijkstra, M. 2014, MNRAS, 444, 1095
Gronke, M., Dijkstra, M., McCourt, M., & Oh, S. P. 2016, ApJL, 833, L26
Gronke, M., Dijkstra, M., McCourt, M., & Oh, S. P. 2017, A&A, 607, A71
Gronke, M., & Oh, S. P. 2020, MNRAS, 492, 1970
Gurung-López, S., Gronke, M., Saito, S., Bonoli, S., & Orsi, Á. A. 2022, MNRAS, 510, 4525
Hansen, M., & Oh, S. P. 2006, MNRAS, 367, 979
Hartmann, D., & Burton, W. B. 1997, Atlas of Galactic Neutral Hydrogen (Cambridge: Cambridge Univ. Press)
Hayes, M., Östlin, G., Duval, F., et al. 2014, ApJ, 782, 6
Hayes, M., Östlin, G., Schaerer, D., et al. 2013, ApJL, 765, L27
Hayes, M. J., Runnholm, A., Scarlata, C., Gronke, M., & Rivera-Thorsen, T. E. 2023, MNRAS, 520, 5903
Hayes, M. J., & Scarlata, C. 2023, ApJL, 954, L14
Heckman, T. M., Borthakur, S., Overzier, R., et al. 2011, ApJ, 730, 5
Heckman, T. M., Lehnert, M. D., Strickland, D. K., & Armus, L. 2000, ApJS, 129, 493
Heintz, K., Watson, D., & Brammer, G. 2023, arXiv:2306.00647
Henry, A., Scarlata, C., Martin, C. L., & Erb, D. 2015, ApJ, 809, 19
Hu, W., Wang, J., Infante, L., et al. 2021, NatAs, 5, 485
Izotov, Y. I., Schaerer, D., Thuan, T. X., et al. 2016, MNRAS, 461, 3683
Izotov, Y. I., Schaerer, D., Worseck, G., et al. 2018a, MNRAS, 474, 4514
Izotov, Y. I., Schaerer, D., Worseck, G., et al. 2020, MNRAS, 491, 468
Izotov, Y. I., Worseck, G., Schaerer, D., et al. 2018b, MNRAS, 478, 4851
James, B. L., Berg, D. A., King, T., et al. 2022, ApJS, 262, 37
Jaskot, A. E., Dowd, T., Oey, M. S., Scarlata, C., & McKinney, J. 2019, ApJ, 885, 96
Jaskot, A. E., & Oey, M. S. 2013, ApJ, 766, 91
Kakiichi, K., & Gronke, M. 2021, ApJ, 908, 30
Kewley, L. J., Nicholls, D. C., & Sutherland, R. S. 2019, ARA&A, 57, 511
Klein, R. I., McKee, C. F., & Colella, P. 1994, ApJ, 420, 213
Kourkchi, E., Courtois, H. M., Graziani, R., et al. 2020, AJ, 159, 67
Kulas, K. R., Shapley, A. E., Kollmeier, J. A., et al. 2012, ApJ, 745, 33
Labbe, I., van Dokkum, P., Nelson, E., et al. 2023, Natur, 616, 266
Leitherer, C., Schaerer, D., Goldader, J. D., et al. 1999, ApJS, 123, 3
Li, Z., & Gronke, M. 2022, MNRAS, 513, 5034
Li, Z., Steidel, C. C., Gronke, M., Chen, Y., & Matsuda, Y. 2022, MNRAS, 513, 3414
Lin, X., Cai, Z., Zou, S., et al. 2023, ApJL, 944, L59
Looser, T. J., D'Eugenio, F., Maiolino, R., et al. 2023, arXiv:2302.14155
Ma, X., Quataert, E., Wetzel, A., et al. 2020, MNRAS, 498, 2001
Martin, C. L., Dijkstra, M., Henry, A., et al. 2015, ApJ, 803, 6
Martin, C. L., Shapley, A. E., Coil, A. L., et al. 2012, ApJ, 760, 127
Martini, P., Leroy, A. K., Mangum, J. G., et al. 2018, ApJ, 856, 61
Mason, C. A., Fontana, A., Treu, T., et al. 2019, MNRAS, 485, 3947
McKinney, J. H., Jaskot, A. E., Oey, M. S., et al. 2019, ApJ, 874, 52
Michel-Dansac, L., Blaizot, J., Garel, T., et al. 2020, A&A, 635, A154
Mingozzi, M., James, B. L., Arellano-Córdova, K. Z., et al. 2022, ApJ, 939, 39
Naidu, R. P., Tacchella, S., Mason, C. A., et al. 2020, ApJ, 892, 109
Nakajima, K., & Ouchi, M. 2014, MNRAS, 442, 900
Neufeld, D. A. 1990, ApJ, 350, 216
Orlitová, I., Verhamme, A., Henry, A., et al. 2018, A&A, 616, A60
Ouchi, M., Ono, Y., & Shibuya, T. 2020, ARA&A, 58, 617
Partridge, R. B., & Peebles, P. J. E. 1967, ApJ, 147, 868
Plat, A., Charlot, S., Bruzual, G., et al. 2019, MNRAS, 490, 978
Prochaska, J. X. 2019, in HI Absorption in the Intergalactic Medium, ed. A. Verhamme et al. (Berlin: Springer), 111
Prochaska, J. X., O'Meara, J. M., Fumagalli, M., Bernstein, R. A., & Burles, S. M. 2015, ApJS, 221, 2
Reddy, N. A., Steidel, C. C., Pettini, M., & Bogosavljević, M. 2016, ApJ, 828, 107
Reddy, N. A., Topping, M. W., Shapley, A. E., et al. 2022, ApJ, 926, 31
Rhoads, J. E., Dey, A., Malhotra, S., et al. 2003, AJ, 125, 1006
Rivera-Thorsen, T. E., Hayes, M., Östlin, G., et al. 2015, ApJ, 805, 14
Robertson, B. E., Ellis, R. S., Furlanetto, S. R., & Dunlop, J. S. 2015, ApJL, 802, L19
Runnholm, A., Gronke, M., & Hayes, M. 2021, PASP, 133, 034507
Saldana-Lopez, A., Schaerer, D., Chisholm, J., et al. 2022, A&A, 663, A59
Saxena, A., Robertson, B. E., Bunker, A. J., et al. 2023, arXiv:2302.12805
Schneider, E. E., & Robertson, B. E. 2018, ApJ, 860, 135
Senchyna, P., Plat, A., Stark, D. P., & Rudie, G. C. 2023, arXiv:2303.04179
Steidel, C. C., Bogosavljević, M., Shapley, A. E., et al. 2011, ApJ, 736, 160
Tang, M., Stark, D. P., Chen, Z., et al. 2023, MNRAS, in press
Tilvi, V., Malhotra, S., Rhoads, J. E., et al. 2020, ApJL, 891, L10
Trainor, R. F., Strom, A. L., Steidel, C. C., et al. 2019, ApJ, 887, 85
Verhamme, A., Dubois, Y., Blaizot, J., et al. 2012, A&A, 546, A111
Verhamme, A., Orlitová, I., Schaerer, D., & Hayes, M. 2015, A&A, 578, A7
Verhamme, A., Schaerer, D., & Maselli, A. 2006, A&A, 460, 397
Xie, Y., Hao, L., & Li, A. 2014, ApJL, 794, L19
Xu, X., Heckman, T., Henry, A., et al. 2022, ApJ, 933, 222
Xu, X., Heckman, T., Henry, A., et al. 2023, ApJ, 948, 28
Yang, H., Malhotra, S., Gronke, M., et al. 2016, ApJ, 820, 130
Yang, H., Malhotra, S., Gronke, M., et al. 2017, ApJ, 844, 171
Yuan, Y., Krumholz, M. R., & Martin, C. L. 2023, MNRAS, 518, 4084
Zheng, Z., Cen, R., Trac, H., & Miralda-Escudé, J. 2010, ApJ, 716, 574
Zheng, Z., Cen, R., Weinberg, D., Trac, H., & Miralda-Escudé, J. 2011, ApJ, 739, 62